8-2018

Measurement and Modeling of Spontaneous Imbibition of Water into Unsaturated, Fractured Low-Porosity Rocks

Jared William Brabazon
University of Tennessee

To the Graduate Council:

I am submitting herewith a thesis written by Jared William Brabazon entitled "Measurement and Modeling of Spontaneous Imbibition of Water into Unsaturated, Fractured Low-Porosity Rocks." I have examined the final electronic copy of this thesis for form and content and recommend that it be accepted in partial fulfillment of the requirements for the degree of Master of Science, with a major in Geology.

Edmund Perfect, Major Professor

We have read this thesis and recommend its acceptance:

Hassina Z. Bilheux, Larry D. McKay

Accepted for the Council:
Dixie L. Thompson

Vice Provost and Dean of the Graduate School

(Original signatures are on file with official student records.)

Measurement and Modeling of Spontaneous Imbibition of Water into Unsaturated, Fractured Low-Porosity Rocks

A Thesis Presented for the
Master of Science
Degree
The University of Tennessee, Knoxville

Jared William Brabazon
August 2018

ACKNOWLEDGEMENTS

I would like to thank my wife Holly for helping me and being by my side throughout my graduate school experience. I would also like to thank my parents for being great examples and encouraging me to work hard.

Thanks to Dr. Edmund Perfect for allowing me this opportunity to work closely with him. I appreciate all the help and guidance he provided me throughout this research. Not only did he help me to learn valuable skills and reasoning, but his character and example were most admirable. Thanks to Dr. Hassina Bilheux and Dr. Larry McKay for offering advice and suggestions while serving on my thesis committee. Thanks to Jean Bilheux for helping with image analysis and processing. I would also like to thank my lab group for helping run samples at Oak Ridge National Laboratory as well as listening to and critiquing my work and presentations. Lastly, I would like to thank the Department of Earth and Planetary Sciences for providing me half GTA support making this experience a reality.

This research was sponsored by the Army Research Laboratory and was accomplished under Grant Number W911NF-16-1-0043. Portions of this research used resources at the High Flux Isotope Reactor, which is a DOE Office of Science User Facility operated by Oak Ridge National Laboratory. The solid-phase density, dry bulk density, and porosity data were collected by A.D. Vial.

ABSTRACT

Spontaneous imbibition (SI) is a capillary-driven flow process, in which a wetting fluid enters a porous medium displacing a preexisting non-wetting fluid. In low-porosity rocks SI generally occurs slowly within the matrix. However, fractured low-porosity rocks allow pathways for rapid SI to occur which can directly influence oil and gas recovery, fracturing fluid loss, leakage from deep waste storage repositories, and the degradation of building materials. Previous research has typically focused on the measurement and modeling of SI in high porosity systems, with little attention given to low-porosity rocks. Furthermore, SI models generally idealize a fracture as a gap formed between parallel flat surfaces, disregarding fracture roughness. Here, a new analytical model was derived for the early-time SI behavior within a fracture bounded by parallel rough fractal surfaces. The model was tested by fitting it to experimental data for the SI of deionized water into air-filled fractures collected on a suite of low-porosity rocks (Burlington Limestone, Crossville Sandstone, Mancos Shale, Sierra White Granite, Vermilion Bay Granite, and Westerly Granite). The SI data were obtained using dynamic neutron radiography at ORNL's Neutron Imaging Facility (beam CG-1D, HFIR). Height of wetting versus time was delineated using change point analysis. The fracture aperture width and fracture sorptivity were also quantified. Among all rock types, geometric mean aperture widths ranged from 84 to 205 μm, with igneous cores producing larger apertures than sedimentary cores. Wetting fronts within the fractures generally exhibited a square-root of time behavior. Fracture sorptivity values ranged from 13.2 to 33.7 $mm \cdot s^{-0.5}$ with sedimentary cores yielding higher values than igneous cores. Differences in fracture surface roughness explained the majority of the variance in the fracture sorptivity values. The newly-derived fractal model fitted the experimental SI data very well for all cores investigated. Inversely estimated surface fractal dimensions, D, all fell within the theoretical bounds of $2 \leq D < 3$, thereby validating this modeling approach for fractured low-porosity rocks. Future research should focus on forward

prediction of SI through independent measurements of D and extension of the fractal SI model to late-times through the inclusion of gravity.

TABLE OF CONTENTS

Chapter 1 Overview of Spontaneous Imbibition within Fractured Porous Media 1
1.1 Introduction 1
1.2 Relevance to Industry etc. 2
1.2.1 Enhanced Oil and Gas Recovery 2
1.2.2 Hydraulic Fracturing “Leakoff” 3
1.2.3 Deep Waste Repositories 4
1.2.4 Damage to Engineered Structures 5
1.3 Goals, Objectives, and Hypotheses 5
Chapter 2 Measurement of Fracture Sorptivity 6
2.1 Introduction 6
2.2 Materials and Methods 7
2.2.1 Rock Cores 7
2.2.2 Core Preparation 9
2.2.3 Measurement of Fracture Aperture Width 9
2.2.4 Dynamic Neutron Radiography 10
2.2.5 Fracture Sorptivity Estimation 11
2.2.6 Statistical Analyses 11
2.3 Results 12
2.4 Discussion and Conclusions 13
Chapter 3 A Fractal Model for Spontaneous Imbibition: Theory and Experimental Validation 17
3.1 Introduction 18
3.2 Theory 19
3.3 Materials and Methods 22
3.4 Results 26
3.5 Discussion and Conclusions 27

Chapter 4 A Fractal Model for Spontaneous Imbibition: Further Experimental Validation 31
4.1 Introduction 31
4.1.1 Carbon Capture and Storage 31
4.1.2 Nuclear and Chemical Deep Waste Repositories 32
4.1.3 Deterioration of Engineered Structures 33
4.3 Materials and Methods 34
4.2 Model Review 36
4.4 Results 37
4.5 Discussion and Conclusions 38
Chapter 5 Conclusions and Suggestions for Future Research 40
5.1 Conclusions 40
5.2 Suggestions for Further Research 42
References 45
Appendices 55
Appendix 1 - Tables 56
Appendix 2 - Figures 64
Vita 83

LIST OF TABLES

Table 1: Physical rock properties of the sample rock types as means of measured values with standard errors shown. Abbreviations of rock types listed below rock name. Note only Mancos Shale (perpendicular) was measured denoted here as simply Mancos Shale. 57

Table 2: Geometric mean aperture width and Tukey's grouping..... 58

Table 3: Sorptivity values for samples with clarity in neutron radiographs allowing hand measurements. Goodness of fit shown by coefficient of determination R^2. Grayed out samples were excluded from further analyses as $R^2 < 0.9$..... 59

Table 4: Mean sorptivity and Tukey's grouping..... 60

Table 5: Parameter estimates and associated 95% confidence intervals obtained by fitting Eq. [3.13] to the neutron radiography data for each replicate of each rock group 61

Table 6: Parameter estimates and associated 95% confidence intervals obtained by fitting Eq. [4.1] to the neutron radiography data for each replicate of each rock group. 62

Table 7: Median values for estimated and measured parameters for all rock cores tested in both chapters 3 and 4. 63

LIST OF FIGURES

Figure 1: Illustration of a porous fractured core coming in contact with a water reservoir over time. T_0 indicates the initial contact of the core with the water reservoir shown on left. Later time steps T_1 and T_2 subsequently shown to the right. Spontaneous imbibition is shown as occurring both within the matrix and within the fracture. Note the difference in wetting front height between the fracture and matrix. 65

Figure 2 : Top view of fractured rock cores. Top row from left to right: Burlington Limestone, Crossville Sandstone, Mancos Shale (cored perpendicular), Mancos Shale (cored parallel); Bottom row from left to right: Vermilion Bay Granite A, Vermilion Bay Granite B, Sierra White Granite, Westerly Granite. 66

Figure 3 : Westerly Granite core with random overlying grid applied to image in ImageJ. Measurements taken at fracture intersection with grid as shown by blue points. Each core had two grids applied per core side resulting in 20 measurements per side and 40 measurements per core. 67

Figure 4 : (a) Neutron radiography imaging set-up with the MCP detector. The rock core (brown) is brought in contact with a water reservoir (aluminum container) in front of the beam-line while the detector images neutrons attenuated by the water. (b) Neutron radiograph produced by the MCP detector of a Crossville Sandstone sample. Note the water reservoir and the linear fracture imbibing water (black). . 68

Figure 5 : Histograms showing the distribution of measured fracture aperture widths for each rock type. X-axis shows aperture width in microns and y-axis shows frequency. Geometric mean aperture width shown as a dotted black line. BL – Burlington Limestone, CS - Crossville Sandstone, MS-par – Mancos Shale (parallel), MS-per – Mancos Shale (perpendicular), SW – Sierra White Granite, VBA – Vermilion Bay

Granite A, VBB – Vermilion Bay Granite B, WG – Westerly Granite. Note the right skewed distributions. 69
Figure 6 : Log-transformed distributions used for analysis of variance. X-axis is the logarithm of the aperture widths in microns. Y-axis represents the frequency. The arithmetic mean of the log distribution is shown as the black dashed line. BL – Burlington Limestone, CS - Crossville Sandstone, MS-par – Mancos Shale (parallel), MS-per – Mancos Shale (perpendicular), SW – Sierra White Granite, VBA – Vermilion Bay Granite A, VBB – Vermilion Bay Granite B, WG – Westerly Granite. 70
Figure 7 : Typical fittings of linear regression per rock type. The coefficient of determination R^2 is shown for each rock type. X-axis represent the square root of time and Y-axis represents the wetting height in mm. The slope of each regression line is equivalent to the respective sample's sorptivity. a) Burlington Limestone; b) Crossville Sandston; c) Mancos Shale (parallel); d) Mancos Shale (perpendicular); e) Sierra White Granite; f) Vermilion Bay Granite A; g) Vermilion Bay Granite B; h) Westerly Granite. 71
Figure 8 : Mean fracture sorptivity with 95% confidence intervals and Tukey letter groupings shown for each rock type. Y-axis is sorptivity in $mm \cdot sec - 0.5$. The arithmetic average of each distribution is shown as a black diamond. Rock types with the same Tukey letter are not significantly different. BL – Burlington Limestone, MS-par – Mancos Shale (parallel), WG – Westerly Granite, MS-per – Mancos Shale (perpendicular), CS - Crossville Sandstone, VBB – Vermilion Bay Granite B, SW – Sierra White Granite, VBA – Vermilion Bay Granite A. 72
Figure 9: Correlation matrix illustrating relationships between sample rock properties. Values of bulk and solid phase density as well as porosity were measured by Andrew Vial. Measurements of contact angle and roughness from Gates (2018). No significant relationship designated by an "X." Positive correlations shown in red with negative correlations shown in blue with gradations in color indicating the

strength of correlation coefficient (r). Significant relationships at p < 0.05 shown with value of correlation coefficient (r). 73
Figure 10: Linear regression relationship between measured fracture sorptivity values and Wenzel surface roughness for all rock types. Roughness measurements from Gates (2018). 74
Figure 11: Core samples ordered from highest sorptivity (top) $\mathrm{mm} \cdot \sec - 0.5$ to lowest (bottom). General qualitative negative correlation shown between increasing grain size and decreasing sorptivity values. Note that this trend seems to fit to all rock types except the Westerly Granite, which has a larger grain size relative to other rock types as well as a higher sorptivity. 75
Figure 12: Minimum contact angles for a fluid on a smooth flat surface, θS, required to give θR > 0 on a rough fractal surface predicted using Eq. [3.7] for various combinations of D and $\ell \mathcal{L}$. 76
Figure 13: Height of wetting within a fracture versus time as predicted by Eq. [3.12]. (a) Fracture aperture spacing, x, held at 100 μm while varying the surface fractal dimension, D. (b) Surface fractal dimension D held at 2.5 while varying the fracture aperture spacing, x. 77
Figure 14 : (a) A typical fractured Mancos Shale (perpendicular) core shown with a superimposed random grid; measurements of aperture width were taken at the intersection points of the fracture and the grid (shown as red dots). (b) Frequency distribution of geometric mean fracture aperture widths for all of the rock types (20 cores) with a bin size of 10 μm; the vertical dashed line represents the median value. 78
Figure 15 : (a) Schematic illustration showing the uptake of water within a fractured core sample soon after basal contact with water. (b) Example of a normalized neutron radiograph showing water (in black) within a fractured Crossville Sandstone core. (c) Change point analysis of the neutron radiograph shown in b. The solid orange lines represent mean pixel values for the wet and dry regions

within the fracture. The blue dashed line is the detection point, representing the height of wetting, at which a shift in the mean pixel values occurred. 79
Figure 16 : Typical height of wetting versus time data sets determined using dynamic neutron radiography and change point analysis: (a) Crossville Sandstone, replicate number 3, and (b) Mancos Shale (cored parallel to bedding), replicate number 2. The solid lines represent predicted values obtained from fitting of Eq. [3.13] to the experimental data using non-linear regression. 80
Figure 17 : Frequency distribution of geometric mean fracture apertures for all of the rock types (24 cores) with a bin size of 20 μm; the vertical dashed line represents the median fracture aperture. 81
Figure 18 : Typical height of wetting versus time data sets determined using dynamic neutron radiography and change point analysis: (a) Burlington Limestone, replicate number 3, (b) Sierra White Granite, replicate number 2, c) Vermilion Bay Granite B, replicate number 11, and d) Westerly Granite, replicate 1. The solid lines represent predicted values obtained from fitting of Eq. [4.1] to the experimental data using non-linear regression. 82

Chapter 1
Overview of Spontaneous Imbibition within Fractured Porous Media

1.1 Introduction

Low-porosity rocks, such as some shales, limestones, and granites, tend to inhibit the flow of fluids. However, these low-porosity rocks, if fractured, allow passageways for potential fluid flow. Many researchers have studied the flow of fluids through fractures within concretes and rocks under pressured, saturated conditions (e.g., Kanematsu et al., 2009; Karpyn et al, 2009; Rangel-German and Kovscek, 2002). However, relatively little research has been done to study the hydraulic properties of fractured low-porosity rocks under partially-saturated conditions.

In unsaturated porous media, a phenomenon known as spontaneous imbibition has the potential to drive fluid flow. Spontaneous imbibition occurs when a wetting phase fluid (e.g., water, brine) moves into a porous medium, displacing the pre-existing non-wetting fluid (e.g., air, natural gas, oil). This process is driven by capillary action within the network of pores (Morrow and Mason, 2001; Schmid et al., 2012).

Many researchers have studied rates of spontaneous imbibition within porous media (e.g., Hall, 1989; Taha et al., 2001; Hanzic and Ilic, 2003). Research has generally focused on construction materials such as mortar, masonry brick, and dry concrete using the rate of spontaneous imbibition as a measure of potential durability (Lockington and Parlange, 2003). However, a recent study by Kang et al. (2013) used neutron radiography to quantify the rate of spontaneous imbibition within a sandstone.

Researchers have shown that spontaneous imbibition is much faster in fractures than in the surrounding matrix (Hall, 2013; Cheng et al., 2015; Tokunaga and Wan, 2001; Şahmaran et al., 2009) (see Figure 1). Cheng et al. (2015) investigated the spontaneous imbibition of water into fractured unsaturated Berea Sandstone cores. These cores ranged in porosities from 19 to 25% and revealed rapid imbibition within the fractured zone relative to the porous matrix. This study focused solely on a high-porosity rock

type. Further research is needed to assess the behavior of spontaneous imbibition within low-porosity fractured rocks, where matrix imbibition is minimal. I hereby seek to extend this previous research by measuring and modeling the spontaneous imbibition of water within fractured unsaturated low-porosity rocks.

1.2 Relevance to Industry etc.

It is important to understand the hydraulic properties of fractured low-porosity rocks, and their influence on spontaneous imbibition rates, as applied to various industrial applications. This phenomenon has been shown to play a role in enhanced oil and gas extraction (Dehghanpour et al., 2013; Morrow et al., 2001), hydraulic fracturing leak-off (Ghanbari et al., 2016), storage of potentially hazardous wastes within the deep vadose zone (Gaurina-Medimurec et al., 2017), and water damage to the foundations of buildings or other engineered structures (Bao et al., 2017).

1.2.1 Enhanced Oil and Gas Recovery

Spontaneous imbibition has long been considered as an important mechanism in enhancing oil recovery in fractured conventional oil and gas reservoirs (Rangel-German and Kovscek, 2002). While the fractures may be significantly more hydraulically conductive than the matrix, often the majority of fluids (e.g. oil, gas) reside in the matrix relative to fractures. Thus, water is typically injected into a fractured reservoir with the intent of allowing spontaneous imbibition to displace the non-wetting phase oil and gas within the pore spaces. The displaced oil and gas can then enter fractures where the fluids can move much more easily than through pore spaces (Rangel-German and Kovscek, 2002). Thus, through the process of spontaneous imbibition, the recovery of oil and gas can be enhanced.

While enhanced oil and gas recovery discussed above focuses primarily on imbibition within the porous matrix, a better understanding the hydraulic properties of fractured low-porosity reservoir rocks and their influence on spontaneous imbibition rates may be of benefit to future oil and gas recovery research within unconventional

reservoirs. Unconventional reservoirs, or oil and gas bearing rock formations with low porosity/permeability, are growing in economic importance. These tight gas shales and sandstones require enhanced recovery methods to be commercially viable. (Cui et al., 2014; Alfarge et al., 2017). The main method used in exploiting these reservoirs is by hydraulic fracturing, also known as "fracking". This method is based on horizontal drilling, and involves the injection of large volumes of water, chemical additives, and suspended solids ("proppants") into the subsurface at high pressures (Osiptsov, 2017). As a result, fractures are induced within the source rocks, increasing their overall permeability (Li et al., 2015). The high rates of flow within the interconnected network of fractures facilitate more efficient recovery of oil and/or gas. Thus, a better understanding of the hydraulic properties of such fractured low-porosity reservoir rocks, and their influence on spontaneous imbibition rates, could aid in enhancing oil and gas recovery.

1.2.2 Hydraulic Fracturing "Leakoff"

As mentioned above, hydraulic fracturing is increasingly being used in fracturing and exploiting low permeability unconventional oil and gas reservoirs. This method requires a large amount of water containing chemical additives and suspended solids (Osiptsov, 2017) to be injected into horizontal wells. Often, only a small fraction of the injected fracturing fluid can be recovered (Ghanbari et al., 2016). This can range from as low as 5% recovered fluid, as seen in the Haynesville Shale, to as high as 50%, as reported in the Barnett and Marcellus Shales (Cheng, 2012; King et al., 2012). This lost fluid is known as "leakoff," and can have potential environmental impacts such as contamination of aquifers (Myers, 2012) and overuse of water resources (Vengosh et al., 2014). Ghanbari et al. (2016) noticed that the leakoff percentage was greatly increased for wells with an extended shut-in time, or when the amount of time the fluid is allowed to sit within the reservoir before initiating flow-back processes. This has been attributed to increased spontaneous imbibition within the reservoir (Ghanbari et al., 2016; Dehganpour et al., 2013). Thus, further measurement and modeling of spontaneous

imbibition within fractured low porosity rocks could provide insight into mitigating or reducing leakoff in unconventional reservoirs.

1.2.3 Deep Waste Repositories

Deep geological repositories are often used to contain unwanted or otherwise harmful substances such as chemical wastes and CO_2 for extended periods of time. Repositories generally consist of natural geologic barriers (e.g. faults, low-permeability layers) bounding a porous storage formation (Suzuki et al., 2018; Gaurina-Međimurec et al., 2017). Often, an overlying low porosity or low permeability layer, referred to as a "caprock," is crucial to the containment of the sequestered waste. In cases of carbon sequestration, a detailed risk assessment is performed in the determination of suitable storage formations and the integrity of caprocks (Intergovernmental Panel on Climate Change, 2005). For nuclear wastes, a combination of low-porosity rocks and engineered materials are used for deep storage (Suzuki et al., 2018). Rather than storing waste in porous rock formations, wastes are encapsulated in an engineered canister and then placed in a shaft within a host rock, typically a granite. A bentonite clay buffer is placed around the canister and is then overlain by a back-fill of clay and host rock material. Lastly, a concrete plug is used to seal the entire storage location (Suzuki et al., 2018; Kim et al., 2011). Several weaknesses such as fractures created during excavation as well as the presence of pre-existing natural fractures may provide potential migration pathways. These migration pathways within a caprock or low-porosity storage site could allow spontaneous imbibition to drive fluid flow of the respective waste, resulting in potential leakage and contamination (Gaurina-Međimurec et al., 2017, Kim et al., 2011). Thus, a better understanding of caprock and low porosity host rock materials, and their response to spontaneous imbibition in fractures, could help mitigate potential contamination and aid in the determination of suitable rock formations for deep waste repositories.

1.2.4 Damage to Engineered Structures

Spontaneous imbibition has been shown to degrade building materials by repeated wetting within microcracks (Bao et al., 2017). As these building materials are rarely fully saturated, spontaneous imbibition is a likely process driving water movement within these fractures. Research has focused on imbibition within materials such as masonry bricks, concretes, mortars, and granites (Bao et al., 2017; Hall, 1989; Taha et al., 2001). Further understanding of common building materials such as granite and limestone and their response to spontaneous imbibition within fractures could aid in the determination of building materials and their overall durability and integrity.

1.3 Goals, Objectives, and Hypotheses

This study focuses on the hydraulic properties of unsaturated, fractured low-porosity rocks. Its main goals are to measure and model spontaneous imbibition of water within individual fractures in such rocks. The objectives of this study are to:

1. characterize the aperture width and tortuosity of fracture damage zones induced by compression of cylindrical rock cores between parallel flat plates
2. visualize the spontaneous imbibition of water within the induced fracture damage zones
3. quantify fracture sorptivity on a suite of low-porosity sedimentary and igneous rocks
4. derive and test a theoretical model for early-time spontaneous imbibition (ignoring gravity) that incorporates fracture surface roughness.

The specific hypotheses to be tested include:

1. rock types will differ in fracture aperture width and tortuosity
2. within the fracture zone, the wetting front will advance with the square-root of time
3. rock types will differ in fracture sorptivity
4. fractal geometry can be used to model fracture surface roughness
5. fracture surface roughness will differ between rock types

Chapter 2
Measurement of Fracture Sorptivity

2.1 Introduction

Spontaneous imbibition occurs when a wetting fluid enters a porous medium and displaces the non-wetting fluid. This process is driven by capillary action within pores (Morrow, 2001; Schmid et al., 2012). It is well known that the wetting height during spontaneous imbibition is related to time by Philip's infiltration equation (Philip, 1957; Cheng et al., 2015):

$$L = C\sqrt{t} \qquad [2.1]$$

In this equation, the height of wetting L is directly proportional to the product of sorptivity C and the square-root of time, t. Thus, the sorptivity is described by the wetting height over the square-root of time. In simple terms, sorptivity is essentially a measure of the rate of imbibition.

Many researchers have investigated spontaneous imbibition in porous media, particularly focusing on measurement of the sorptivity parameter (Cheng et al., 2015; Hall, 1989; Schmid et al., 2012; Taha et al., 2001). The study of sorptivity has shown that it is a useful parameter to quantify the water uptake rate at both the small, individual pore scale, and at larger Darcian, multiple pore, scales (Cheng et al., 2015; Taha et al., 2001).

Sorptivity has been found to be a useful measure of spontaneous imbibition in fractured porous media. Hall (2013) used neutron radiography to qualitatively investigate the spontaneous imbibition of water in fractured porous media, comparing uptake in the fractures themselves with that in the surrounding matrix. It was found that the rate of imbibition was much faster in fractures than in the surrounding matrix (Hall, 2013). Cheng et al. (2015) built upon Hall's findings and developed a theoretical model to quantitatively describe this difference, ultimately allowing the estimation of a sorptivity value for the fracture zone. These authors attributed the increase in

spontaneous imbibition within the fracture zone to early time capillary action, as well as surface spreading along the rough fracture surface (Cheng et al., 2015).

Here I seek to measure spontaneous imbibition within the fracture zone of several types of low-porosity fractured rocks. The fracture sorptivity will be quantified for each respective rock type as a means to better understand potential differences in rates of imbibition among rock types.

2.2 Materials and Methods

2.2.1 Rock Cores

Low-porosity rock cores were acquired from Kocurek Industries Inc. (Caldwell, TX), a commercial vendor. Several replicate cores were obtained for each rock type, allowing for a statistical analysis of the dataset. As similar rock types were used for experiments outlined in Chapter 2 (i.e. fracture sorptivity measurement) and in Chapters 3 and 4 (i.e. spontaneous imbibition model validation), it is to be noted that different cores were used for each respective experiment. All cores were 5.08 cm long by 2.54 cm in diameter and were obtained from surface outcrops with unknown locations (see Figure 2 for photographs of each core's cross-section). The acquired cores consisted of both sedimentary and igneous rock types. The sedimentary cores included Burlington Limestone, Crossville Sandstone, and Mancos Shale (cored perpendicular to bedding). The igneous cores consisted of a suite of granites including Vermilion Bay Granite A, Vermilion Bay Granite B, Sierra White Granite, and Westerly Granite.

Burlington Limestone (known commercially as "Carthage Marble") is a fine-grained, gray to brown crystalline limestone. The permeability of Burlington Limestone varies between 4×10^{-18} and 7×10^{-18} m^2 as described by Kocurek Industries Inc. Crossville sandstone (known commercially as "Crab Orchard sandstone") was deposited during the Pennsylvanian period and is located in Kentucky and Tennessee, USA. It is a light-gray fine- to medium-grained sandstone with bands of red, yellow, brown and gray due to iron staining (Wanless, 1946). The permeability of Crossville sandstone varies

between 3×10^{-18} and 3×10^{-17} m^2 (Gehne and Benson, 2017). The Mancos shale is an interbedded siltstone and shale located in New Mexico, Wyoming, and Utah, USA. It was deposited during the Late Cretaceous and has an estimated 595 billion cubic meters of recoverable gas (McLennan et al., 1983; U.S. Energy Information Administration, 2011). Its permeability varies between 3×10^{-17} and 9×10^{-19} m^2 (Mokhtari and Tutuncu, 2015). The Mancos samples were gray in color with light gray inter-bedding. Samples were taken both cored parallel and perpendicular to the bedding planes.

Sierra White Granite is a granodiorite that was emplaced between the Permian and Tertiary periods (Jennings et al., 1977). Both Vermilion Bay Granite A and Vermilion Bay Granite B (known commercially as “Morning Rose” Granite and “North American Pink” Granite, respectively) are fine grained deep pink to light red alkali granites from Northwestern Ontario, Canada. Westerly Granite is a fine grained gray to light gray granite located in Rhode Island, USA. It was likely emplaced in the Pennsylvanian period and ranges in composition from quartz monzonite to granodiorite. The granite is equigranular with an average grain size of 0.75 mm and a typical modal composition of 28% quartz, 36% potassium feldspar, 31% plagioclase, and 5 % biotite (Wawersik and Brace, 1970; Quinn, 1971). The permeability of Westerly Granite is 6×10^{-20} m^2 (Brace et al., 1968).

The bulk density, solid phase density, and helium gas porosity of the cored samples were measured by Andrew Vial using the method of Donnelly et al. (2016). Intrinsic contact angles for deionized-water on polished flat surfaces of the different rock types were measured using the sessile drop method by Gates (2018). Wenzel roughness factors from the well-known Wenzel (1936) equation for the rock fracture surfaces, further referenced here as surface roughness, were measured using a Phenom Pro X scanning electron microscope (Phenom-World B.V., Eindhoven, Netherlands) by Gates (2018). Selected mean physical properties for the different rock types are given in Table 1.

2.2.2 Core Preparation

Prior to neutron radiography, all of the cores were oven dried at 105°C for a period of 24 hours to bring each core to a zero initial moisture content (Ulusay and Hudson, 2007). Cores were then wrapped using Kapton® Tape. This ensures no-flow boundaries and helps to keep the fractured sample intact. Such tape is free of hydrogen compounds which would otherwise inhibit the ability to effectively image the imbibition of water using neutron imaging. The wrapped cores were then fractured using the Brazilian method which involves inducing a mode-I fracture, by applying a stress to the core as it is placed between parallel loading plates (Li et al., 2013, Cheng et al., 2015)(refer to Figure 2 for cross-sectional views of the fractured cores). This was accomplished using a Carver Laboratory Press (Model M) with a 25 Ton Hydraulic Unit (Model #3925). The fractured cores were then placed into a humidity controlled container to minimize changes in their moisture content over time.

2.2.3 Measurement of Fracture Aperture Width

Fracture apertures, acting somewhat like capillary tubes, likely influence rates of water imbibition into the cores. As seen in porous media, faster early time imbibition of the wetting phase is seen in larger capillaries, while slower imbibition is seen in smaller capillaries (Shi et al., 2018). Thus, all fractured cores were characterized by their aperture widths to account for this potential influence.

Images of both the bottom and top of the fractured core were taken with a high-resolution camera. These images were then cropped to allow the edge of the image to be tangential to the edge of the core. Conversion from pixels to microns was achieved by measuring the dimensions of the cropped images in ImageJ (Schneider, 2012) and assuming the diameter of the cores to be exactly 25.4 mm. The width of the aperture was measured at 10 locations on a randomly-positioned superimposed square grid in ImageJ (see Figure 3). The measurement process was then repeated using a second randomly-positioned grid. Both the top and bottom images of the core were analyzed in this way, resulting in 40 aperture width measurements per core.

2.2.4 Dynamic Neutron Radiography

Spontaneous imbibition data, or the height of wetting at a given time within the fracture zone, were obtained for each rock-type. Neutron radiography is a novel way to obtain these data due to its ability to image the uptake of water within a fracture at reasonable frame rates. Neutron imaging was performed at the Neutron Imaging Facility (beam line CG-1D, HFIR) at ORNL. Data were collected in May 2017 utilizing the MCP detector. This detector has a pixel size of 55 μm and a field of view of 28 x 28 mm^2 (see Figure 4a). The detector yielded a relatively consistent frame rate of ~6 frames per second.

To perform neutron radiography, the prepared oven-dried cores were placed individually in front of the neutron detector with the fracture plane parallel to the neutron beam-line. The cores were imaged while their bases were brought into contact with a deionized-water reservoir. The resulting imbibition within the fracture zone was visualized as a series of time-stamped radiographic images.

Images from each core were analyzed to delineate the height of the wetting front with respect to time. In ImageJ, (Schneider, 2012), images were first normalized to more easily see the uptake within the fracture zone. The normalization was done by dividing each image in the time sequence by the initial image before water contacted the base of the core. As no electronic noise is produced by the MCP detector, this process of normalization can be used effectively. Resulting normalized images allow for the delineation of the wetting front within the fracture zone at any given time (see Figure 4b). Once normalized, the core width (in pixels) was determined by three random measurements of the core within the image. Knowing the core width to be 25.4 mm, the average pixel length of the core width was converted to millimeters. Using this conversion, the visible rise in uptake for each image in the sequence was measured three times in ImageJ and then averaged yielding the height of wetting in millimeters for each respective time.

2.2.5 Fracture Sorptivity Estimation

Due to the rapidity of the spontaneous imbibition phenomenon, coupled with the relatively low frame rate of the MCP detector, only between 3 and 11 pairs of wetting height and corresponding time values were obtained for each core. To see how the different rock-types compare in their fracture imbibition rates, fracture sorptivity values were quantified from the data collected. This was accomplished by first plotting the square-root of time as the independent variable and the height of wetting as the dependent variable for each respective core. If a linear relationship existed between these variables, then the fracture sorptivity was obtained by linear regression, with the slope of the linearly regressed line forced through the origin denoting the fracture sorptivity (Culligan et al., 2005; Taha et al., 2001). The coefficient of determination, R^2, was used to assess the strength of the linear relationship. If the R^2 was less than 0.9, showing a relatively poor linear relationship between the height of wetting versus the square-root of time, the resulting fracture sorptivity value was excluded from further analyses.

2.2.6 Statistical Analyses

Analyses of variance (ANOVA) were performed on the measured aperture widths and the calculated fracture sorptivity values to compare mean values between rock types. Post hoc Tukey HSD (honestly significant difference) tests were used to test equivalency of mean values between pairs of rock types. Relationships between variables such as mean sorptivity, geometric mean aperture width, mean bulk density, average contact angle, average solid phase density, mean porosity, and mean fracture roughness were explored using correlation coefficients (r) among rock types. It is to be noted that many of these values were not measured for the Mancos Shale (parallel) cores. Thus, this rock type was excluded from the correlation investigation. Statistical significance was assessed at the $p < 0.05$ level. Due to limited number of observations, p-values for the correlations were not corrected for multiple comparisons. All of the statistical analyses were performed in the R software environment (R Core Team, 2016).

2.3 Results

The distributions of the aperture widths were right skewed for all rock types (see Figure 5). For statistical analysis, aperture width data were log-transformed to satisfy ANOVA assumptions (Figure 6). Analysis of variance performed on the log-transformed values indicated significant differences (at $p < 0.05$) among the rock types. The results were then back-transformed to give geometric mean aperture widths. Among all rock types, the geometric mean aperture width ranged from 84 to 205 μm (Table 2). Post hoc comparisons using the Tukey HSD indicated four groupings with statistically similar geometric mean aperture widths among the rock types (see Table 2).

Height of wetting within the fracture consistently portrayed a square-root of time behavior (Figure 7). Sorptivity values were quantified from the slopes of regression lines fitted to the height versus square root of time data from the neutron imaging measurements. Typical fits and regression models are shown in Figure 7. After removing fits with R^2 values < 0.9 shown in table 3, sorptivity values were averaged over several replicate cores per rock type, and are given in Table 4.

Among rock types, sorptivity values ranged from 13.2 to 33.7 $mm \cdot s^{-0.5}$ with an overall average of 24.1 $mm \cdot s^{-0.5}$. ANOVA indicated significant differences in average sorptivity values among rock types (at $p < 0.05$). Based on the Tukey HSD test, four groupings with statistically similar mean sorptivity values were distinguished among rock types (see Table 4 and Figure 8).

Statistically significant relationships (at $p < 0.05$) were found between geometric mean aperture width and porosity as well as between geometric mean aperture width and bulk density. Geometric mean aperture widths were negatively correlated to porosity and positively correlated to bulk density. Sorptivity was negatively correlated with the Wenzel roughness factor (see Figure 9).

2.4 Discussion and Conclusions

As can be seen in Table 2, the igneous rocks generally produced larger aperture widths, with geometric means ranging from 125 to 205 μm, relative to the sedimentary samples. Among igneous rocks, Westerly Granite yielded the largest aperture width, followed by Sierra White Granite, and Vermilion Bay Granite A, with geometric means of 205, 176, and 166 μm, respectively. The Vermilion Bay Granite B produced the smallest aperture among igneous rocks with a geometric mean aperture width of 125 μm. The sedimentary rocks generally had narrower aperture widths, with geometric means for the sandstone and shales ranging from 84 to 89 μm. The Burlington Limestone, however, yielded wider fracture apertures than the other sedimentary rocks, and even the majority of igneous rocks, with a geometric mean aperture of 191 μm. This distinction among igneous and sedimentary rocks in aperture width could potentially be due to differences in porosity as indicated by the correlation coefficient (r) in Figure 9. As indicated by the negative correlation between geometric mean aperture width and porosity, wider fractures were generally produced in lower porosity rocks. As porosity increases, the presence of larger void spaces may alter the width of an induced fracture. The positive correlation between geometric mean fracture width and solid phase density (Figure 9) indicates that mechanical properties related to the mineralogy of the rock may also play a potential role in influencing the width of the fracture aperture.

Mean fracture sorptivity values ranged from 13.2 $mm \cdot s^{-0.5}$ to 33.7 $mm \cdot s^{-0.5}$ (Table 4). Although no significant correlation existed between sorptivity and fracture aperture width, the igneous cores, which generally had larger aperture widths, tended to have lower sorptivity values (refer to Figure 8). The Westerly Granite, however, yielded a much higher sorptivity relative to the other granites. The sedimentary cores, having a relatively smaller aperture width, tended to have higher sorptivity values. Shi et al. (2018) suggested that pores with greater widths should imbibe faster than pores of a smaller width within a porous material. It seems that within fracture zones, however, this trend does not always hold true. Here the Mancos Shale (parallel) had nearly the

smallest aperture width, but yielded nearly the highest sorptivity. It seems that other factors, such as contact angle and fracture surface roughness, may play a larger role in influencing the fracture imbibition rate.

This can be seen from the correlation coefficient (r) in Figure 9, indicating a negative correlation between fracture sorptivity and Wenzel roughness factor. This indicates that fracture sorptivity tends to decrease as roughness increases among these rock types as shown in Figure 10. In general, among the given rock types, granites tend to be rougher, yielding relatively lower fracture sorptivity. Sedimentary rocks tend to have less roughness relative to granites and yield higher fracture sorptivity. To my knowledge, no studies have focused on the influence of fracture surface roughness on spontaneous imbibition within fracture zones. Many studies have focused on the influence of fracture surface roughness on fluid flow in saturated conditions where the hydrostatic pressure is greater than atmospheric pressure (Koyama et al., 2008; Huang et al., 2017; Huang et al., 2018). For example, Huang et al. (2018) noticed that the flow path inside rough fractures shear bands greatly reduces permeability in saturated conditions. Because of this, fluid flow tends to disperse into pathways perpendicular to the rough fracture path where permeability can be much larger (Huang et al., 2018). Similarly, Brown (1987) noted that flow through rough fracture surfaces yielded flow rates between 70 and 90% of that estimated from models incorporating smooth parallel plate fractures. Thus, we see that under saturated conditions, roughness tends to slow fluid flow within the fracture zone.

In the current study, a zero gauge pressure is used where fluid flow is driven by capillary action. While this study was not performed under saturated flow, similar principles likely apply in regards to the influence of roughness on fluid flow. Here, low-porosity rocks were used, which inhibit imbibition perpendicular to the fracture during early time spontaneous imbibition. Thus, fracture spontaneous imbibition is restricted to the fracture zone. Much like that seen in saturated flow, as the roughness of the fracture surface increases, perhaps, the pathway inside the rough fracture decreases

permeability and increases tortuosity relative to that of smoother fractures. As the porosity of the rocks is quite low, spontaneous imbibition is focused only within the rough fracture zone, with no potential for lateral dispersion. Thus, the increased fracture surface roughness has potential to yield a lower relative sorptivity.

A recent study by Vogler et al. (2017) suggested that the Brazilian test, a test to produce tensile fractures by exceeding the tensile strength of the rock, produced mode-I fractures dominated by intragranular cracks in smaller core sizes (diameter < 2.5cm). On a small scale, the intragranular cracks tend to form jagged surfaces, increasing roughness (Vogler et al., 2017). In the present study, relatively small core sizes were employed, thus intragranular cracks may be the dominant way in which tensile fractures were produced rather than following grain boundaries. Thus, surface roughness may be increased in samples in which intragranular cracks dominate. These intragranular cracks were clearly seen within the larger grained granite cores. Qualitatively, cores with smaller grain sizes seem to have increased sorptivity values (see Figure 11). Perhaps, among these cores, those with smaller grain sizes tend to produce fractures that follow grain boundaries while cores with larger grains tend to produce jagged fractures from intragranular cracks. This potential difference in roughness may explain some of the observed differences in sorptivity.

Lastly, another potential driver in determining rates of fracture imbibition is chemical composition, and its effect on contact angle. Overall, there was no significant relationship between intrinsic contact angle and fracture sorptivity (Figure 9). However, the Vermilion Bay Granites and the Sierra White Granite all have relatively similar chemical compositions. According to the Tukey HSD test, these samples group together sharing lower sorptivity values (refer to Figure 8). The Westerly Granite is, however, anomalously higher in sorptivity. Thus, it seems that an interplay of both surface fracture roughness and mineralogy of the rock types play a large role in influencing spontaneous imbibition within the fracture zone. Future studies of this nature should include a larger number of samples of diverse rock types to provide a more robust

statistical evaluation of relationships between fracture sorptivity and physicochemical properties.

Chapter 3
A Fractal Model for Spontaneous Imbibition: Theory and Experimental Validation

A slightly modified version of this chapter has been accepted for publication in the journal, Fractals: Brabazon, J.W., E. Perfect, C.H. Gates, L.J. Santodonato, I. Dhiman, H.Z. Bilheux, J.-C. Bilheux, and L.D. McKay. 2018. Spontaneous Imbibition of a Wetting Fluid into a Fracture with Opposing Fractal Surfaces: Theory and Experimental Validation. Fractals. (in press).

Spontaneous imbibition (SI) is a capillary-driven flow process, in which a wetting fluid moves into a porous medium displacing an existing non-wetting fluid. This process likely contributes to the loss of fracking fluids during hydraulic fracturing operations. It has also been proposed as a method for enhanced recovery of hydrocarbons from fractured unconventional reservoirs. Numerous analytical and numerical approaches have been employed to model SI. Invariably, these idealize a fracture as the gap formed between parallel flat surfaces. In reality, rock fracture surfaces are rough over multiple scales, and this roughness will influence the contact angle and rate of fluid uptake. We derived an analytical model for the early-time SI behavior within a fracture bounded by parallel impermeable surfaces with fractal roughness assuming laminar flow. The model was tested by fitting it to experimental data for the SI of deionized water into air-filled rock fractures. Twenty cores from 2 rock types were investigated: a tight sandstone (Crossville) and a gas shale (Mancos). A simple mode-I longitudinal fracture was produced in each core by compressive loading between parallel flat plates using the Brazilian method. Half of the Mancos cores were fractured perpendicular to bedding, while the other half were fractured parallel to bedding. The two main parameters in the SI model are the mean separation distance between the fracture surfaces, $\bar{x}$, and the fracture surface fractal dimension $2 \leq D < 3$. The $\bar{x}$ was estimated for each core by measuring the geometric mean fracture aperture width through image analysis of the top and bottom faces, while D was estimated inversely by fitting the SI model to

measurements of water uptake obtained using dynamic neutron radiography. The $\bar{x}$ values ranged from 45 to 190 μm, with a median of 93 μm. The SI model fitted the height of uptake versus time data very well for all of the rock cores investigated; medians of the resulting root mean squared errors and coefficients of determination were 0.99 mm and 0.963, respectively. Estimates of D ranged from 2.04 to 2.45, with a median of 2.24. Statistically, all of the D values were significantly greater than two, confirming the fractal nature of the fracture surfaces. Future research should focus on forward prediction through independent measurements of D and extension of the existing SI model to late times (through the inclusion of gravity) and fractures with permeable surfaces.

3.1 Introduction

Unconventional reservoirs are oil and/or gas producing rock formations that require the implementation of enhanced recovery methods to be commercially viable. They include low permeability gas shale's and tight gas sandstones, and are of growing economic importance (Cui et al., 2014; Alfarge et al., 2017). The development of hydraulic fracturing, or "fracking," technology has been the key to exploiting unconventional reservoirs. This method is based on horizontal drilling, and involves the injection of large volumes of water, chemical additives, and suspended solids ("proppants") into the subsurface at high pressures (Osiptsov, 2017). As a result, fractures are induced within the source rocks, increasing their overall permeability (Li et al., 2015). The high rates of flow within the interconnected network of fractures facilitate more efficient recovery of oil and/or gas.

Spontaneous imbibition is a capillary-driven flow process, in which a wetting fluid (e.g., water, brine) moves into a porous medium displacing a preexisting non-wetting fluid (e.g., air, natural gas, oil) (Mason and Morrow, 2013; Meng et al., 2017). This process, using water or brine with added surfactants to displace oil, has been proposed as an enhanced recovery technique (Babadagli, 2005; Towler et al., 2017).

With the rapid growth and implementation of fracking technology, spontaneous imbibition is now being investigated as a method of improving the recovery of hydrocarbon resources from fractured unconventional reservoirs (Fernø, 2012; Javaheri et al., 2017). Spontaneous imbibition may also contribute to the loss of fracking fluids (known as "leakoff") during hydraulic fracturing operations. (Dehghanpour et al., 2013).

Numerous analytical and numerical approaches have been proposed for modeling the spontaneous imbibition of a wetting fluid into the gap formed by parallel planar surfaces (e.g., Schwiebert and Leong, 1996; Xiao et al. 2006; Wang et al., 2017). However, these models invariably represent the opposing surfaces of the fracture as smooth and flat. In reality, rock fracture surfaces are rough over multiple scales, and this roughness likely influences the contact angle and rate of fluid uptake within the fracture. Fractal geometry is a quantitative paradigm for simulating and characterizing the irregularity of natural systems (Mandelbrot, 1982). Cai (2010) developed a fractal model to predict the displacement of a non-wetting fluid by a wetting fluid within a tortuous capillary tube. Several studies have shown that rock fracture surfaces exhibit fractal roughness over length scales of two or more orders of magnitude (Power et al., 1991; Develi and Babadagli, 1998; Boffa et al., 1998; Babadagli and Develi, 2003). However, we were unable to find any previously published studies that have sought to incorporate the fractal roughness of fracture surfaces into a model for the prediction of spontaneous imbibition.

The objective of this paper, is to derive an analytical model for the spontaneous imbibition mechanism within a fracture bounded by parallel rough fractal surfaces. The model will be tested by fitting it to experimental data for the spontaneous imbibition of water into air-filled fractured rock cores collected using neutron radiography.

3.2 Theory

The well-known Wenzel (1936) equation for the contact angle of a fluid on a rough surface, θ_R, is given by:

$$cos\theta_R = r cos\theta_S \quad [3.1]$$

where θ_S = the contact angle of a fluid on a smooth flat surface, and r is the roughness ratio, defined as:

$$r = \frac{A_R}{A_S} \quad [3.2]$$

where A_R = the projected area of the rough surface relative to the corresponding area of the smooth flat surface, A_S.

Assuming the rough surface is fractal, the number, N, of tiles of length, ℓ, needed to cover it can be calculated using the following expression (Russ, 1994; Turcotte, 1997):

$$N = \left(\frac{\mathcal{L}}{\ell}\right)^D \quad [3.3]$$

where $\mathcal{L}$ = the length scale corresponding to the maximum extent of fractal scaling, and $2 \leq D < 3$ is the surface fractal dimension. Based on Eq. [3.3], the area of a rough fractal surface of length $\mathcal{L}$ is given by:

$$A_R = \ell^2 N = \ell^{2-D}\mathcal{L}^D \quad [3.4]$$

Based on Euclidean geometry, the area of a smooth flat surface of length $\mathcal{L}$ is given by:

$$A_S = \mathcal{L}^2 \quad [3.5]$$

Substituting Eqs. [3.4] and [3.5] into Eq. [3.2] we obtain:

$$r = \left(\frac{\ell}{\mathcal{L}}\right)^{2-D} \quad [3.6]$$

Substituting Eq. [3.6] into Eq. [3.1] we obtain the following expression for the contact angle of a fluid on a rough fractal surface:

$$cos\theta_R = \left(\frac{\ell}{\mathcal{L}}\right)^{2-D} cos\theta_S \quad [3.7]$$

Eqs. [3.1] through [3.7] provide a new, parsimonious derivation of Hazlett's (1990) equation for the contact angle of a fluid on a rough fractal surface. Hazlett's (1990) equation was written in terms of area scaling limits instead of length scaling limits, i.e.

$$cos\theta_R = \left(\frac{\sigma_L}{\sigma_U}\right)^{1-\frac{D}{2}} cos\theta_S \quad [3.8]$$

where σ_U and σ_L are the upper and lower area limits of fractal scaling, respectively. Comparing Eqs. [3.7] and [3.8] it can easily be seen that they are equivalent, since $\sigma_U \propto \mathcal{L}^2$ and $\sigma_L \propto \ell^2$

Ignoring gravity, the spontaneous imbibition of a wetting fluid into the gap formed between smooth flat impermeable parallel plates is given by (Schwiebert and Leong, 1996):

$$L = \sqrt{\frac{x\gamma cos\theta_S t}{3\mu}} \qquad [3.9]$$

where L = the distance travelled by the wetting front in time, t, x = the separation distance between the two plates, μ = the absolute viscosity, and γ = the surface tension of the liquid-vapor interface. Substituting Eq. [3.7] into Eq. [3.9] and replacing x with the mean separation distance between the fracture surfaces, $\bar{x}$ (Brown, 1987), results in the following expression for the spontaneous imbibition of a wetting fluid into the gap formed by parallel impermeable fracture surfaces with fractal roughness:

$$L = \sqrt{\frac{\bar{x}\gamma\left(\frac{\mathcal{L}}{\ell}\right)^{2-D} cos\theta_R t}{3\mu}} \qquad [3.10]$$

Both Eqs. [3.9] and [3.10} assume a laminar flow regime.

It is evident from Eq. [3.7] (see Figure 12), that the contact angle for a wetting fluid on a rough fractal surface (θ_R) tends to approach zero for most values of θ_S, D and $\frac{\ell}{\mathcal{L}}$ likely to be encountered in geological systems. Thus, it is reasonable to assume that $cos\theta_R$ = 1 in Eq. [3.10], i.e.

$$L \approx \sqrt{\frac{\bar{x}\gamma\left(\frac{\mathcal{L}}{\ell}\right)^{2-D} t}{3\mu}} \qquad [3.11]$$

Assuming that the distance travelled by the wetting front represents the upper length limit of fractal scaling, i.e. $L = \mathcal{L}$, Eq. [3.11] can be rewritten as:

$$L \approx \left(\frac{\bar{x}\gamma}{3\mu\ell^{2-D}}\right)^{\frac{1}{D}} t^{\frac{1}{D}} \qquad [3.12]$$

The influence of the surface fractal dimension, D and mean fracture aperture width, $\bar{x}$, on rates of water uptake predicted by Eq. [3.12] are illustrated in Figure 13. When $\bar{x}$ is held constant, imbibition rates decrease with increasing values of D (Figure 13a); this trend can be attributed to the increase in surface roughness as D gets larger, resulting in more tortuous flow paths, and possibly turbulent flow (Wang et al., 2016), within the fracture. As $\bar{x}$ is increased with D held constant, imbibition rates increase (Figure 13b); this is because flow occurs more easily within a wider channel due to reduced friction with the side walls. It should be noted that these are early time predictions, because the current model neglects gravity. As such they are consistent with standard capillary theory, which predicts rapid rates of uptake in large diameter capillary tubes at early times, but lower maximum heights attained relative to smaller diameter capillary tubes at late times (Cheng et al., 2015).

When applying Eq. [3.12] in an experimental setting, neutron radiography is used to determine L and t (see Materials and Methods). However, the time at which the wetting fluid first contacts the base of the fracture is not known precisely. Therefore, when fitting Eq. [3.12] to experimental data a constant, c, is introduced to account for this uncertainty, i.e.

$$L \approx \left(\frac{\bar{x}\gamma}{3\mu\ell^{2-D}}\right)^{\frac{1}{D}}(t-c)^{\frac{1}{D}} \qquad [3.13]$$

The unknown parameters, to be estimated by fitting Eq. [3.13] to experimental L versus t data, are D and c. The other parameters in Eq. [3.13], γ, μ, $\bar{x}$ and ℓ, are all known quantities; γ and μ are physico-chemical constants whose values are available in tables, $\bar{x}$ is measured by image analysis (see Materials and Methods), and the lower length limit of fractal scaling, ℓ, is taken to be the length of the ruler used for the measurements, i.e. pixel length in neutron radiography.

3.3 Materials and Methods

Two rock types with physical properties representative of unconventional reservoir rocks were investigated: a tight sandstone (Crossville) and a gas shale

(Mancos). Several core samples (5.08 cm long × 2.54 cm diameter) of each rock type were supplied by Kocurek Industries Inc. (Caldwell, TX, USA). The samples were cored from surface outcrops with unknown locations. The Crossville sandstone samples were cored parallel to bedding, while the Mancos shale samples were cored both parallel and perpendicular to bedding.

Crossville sandstone (known commercially as "Crab Orchard sandstone") was deposited during the Pennsylvanian period and is located in Kentucky and Tennessee, USA. It is a light-gray fine- to medium-grained sandstone with bands of red, yellow, brown and gray due to iron staining (Wanless, 1946). The permeability of Crossville sandstone varies between 3×10^{-18} and 3×10^{-17} m^2 (Gehne and Benson, 2017). The solid phase density and helium gas porosity of the cored samples were measured using the method of Donnelly et al. (2016) and were determined to be 2.50 ($\pm$0.01) g cm^{-3} and 5.85 ($\pm$0.27) %, respectively.

The Mancos shale is an interbedded siltstone and shale located in New Mexico, Wyoming, and Utah, USA. It was deposited during the Late Cretaceous and has an estimated 595 billion cubic meters of recoverable gas (McLennan et al., 1983; U.S. Energy Information Administration, 2011). Its permeability varies between 9×10^{-19} and 3×10^{-17} m^2 (Mokhtari and Tutuncu, 2015). The Mancos samples were gray in color with light gray inter-bedding. Their solid phase densities and helium gas porosities were determined, using the method of Donnelly et al. (2016), to be 2.50 ($\pm$0.01) g cm^{-3} and 5.59 ($\pm$0.39) %, respectively.

Each rock core was wrapped longitudinally with Kapton® tape to help maintain the integrity of the sample during fracturing and to create a no-flow boundary for the water uptake experiments. This tape can withstand high temperatures and high pressures, and is free of hydrogen compounds that would otherwise inhibit the neutron radiography. A simple mode-I longitudinal fracture was produced in each wrapped core by compressive loading between parallel flat plates using the Brazilian method (Li and Wong, 2013; Cheng et al., 2015). The load was applied by manually

operating the bottom loading platen of a Carver Laboratory Press (Model M) with a 25 Ton Hydraulic Unit (Model #3925). A distinctive crack sound was heard as soon as the fracture occurred. Loading was then immediately stopped.

Fracture aperture widths were measured on all of the cores. Images of both the top and bottom faces of each fractured core were taken with a high resolution camera. These images were analyzed using ImageJ (Schneider et al., 2012). The width of the aperture was measured at 10 locations on a randomly-positioned superimposed square grid (see Figure 14a). The measurement process was then repeated using a second randomly-positioned grid. Both the top and bottom images were analyzed in this way, resulting in 40 width measurements per core. As observed by other researchers (e.g., Keller, 1998; Konzuk and Kueper, 2004), these data were log-normally distributed. Therefore, the geometric mean fracture aperture width was used as the best estimator of $\bar{x}$ for each core.

Prior to the spontaneous imbibition experiments all of the cores were oven dried at 105°C for a period of 24 hours to bring them to a zero initial moisture content. The oven-dried cores were then placed into a humidity controlled container to prevent changes in the core's moisture content prior to placement in the neutron beam.

As shown in previous studies (e.g., Cheng et al., 2015; Perfect et al., 2014), neutron imaging allows for distinct visualization of the movement of hydrogen-rich liquids within rocks and other porous media. Thus, dynamic neutron radiography was employed to measure the spontaneous imbibition of water within the fractured rock cores. The imaging was performed at Oak Ridge National Laboratory's Neutron Imaging Facility (beam line CG-1D, HFIR). The configuration and specifications of this cold neutron beam line are described in Santodonato et al. (2015). Neutron radiographs were obtained using the sCMOS detector at a rate of 30 frames per second. The field of view was 28 mm x 28 mm, and the spatial resolution was 100 μm. Cores were placed individually in front of the sCMOS detector with their fracture planes oriented parallel to the neutron beam. Each core was imaged as it was brought into contact with a

deionized-water reservoir following Cheng et al. (2015) (Figure 15a). The resulting uptake of water within the fracture was imaged as a series of time-stamped neutron radiographs.

The radiographs were normalized to ensure visualization of the water (shown as black pixels). To do this, dark-field images were subtracted from radiographs captured both prior to and during wetting. The resulting wetting images were then divided by one of the dry images yielding the final normalized radiographs for each core (Figure 15b). For each time series of normalized radiographs, a 50 pixel wide transect was superimposed over the fracture from the base of the core to the top of the image. The fracture transect was segmented so as to closely follow any deviations from linearity in the fracture. The total length of the transect, L_T, was then used to compute the fracture tortuosity, τ, using the relationship $\tau = \frac{L_T}{L_S}$, where L_S is the straight line distance between the two ends of the transect.

Pixel gray-scale values were averaged over the width of each superimposed transect, resulting in an average gray-scale pixel value for each pixel length of the transect (Figure 15c). Change point analysis was employed to determine L by detecting the distance the water had moved along the transect in each normalized neutron radiograph. Change point analysis can identify abrupt shifts in the statistical properties of a sequence of observations (Eckley et al., 2011). It is widely used in such fields such as climatology, bioinformatics, and finance (Beaulieu et al., 2012; Reeves et al., 2007; Erdman and Emerson, 2008; Zeileis et al., 2010). We used a single change point model with a likelihood-ratio based approach, as described by Eckley et al. (2011), to detect specific shifts in the mean and variance of the average gray-scale pixel values along the fracture transect. The resulting change point for each radiograph in the time series is a mathematical representation of the distance the water has imbibed along the fracture (Figure 15c). The change points were converted from pixel values to millimeters by comparing the measured diameter of the core in the radiograph to its known diameter. Corresponding t values were extracted from the radiograph time stamps.

Between 16 and 60 pairs of L and t values were collected for each core (Table 5). The surface fractal dimension, D, and initial imbibition time, c, were estimated by fitting Eq. [3.13] to the experimental L and t values on a core-by-core basis, with all other parameters specified, using the Levenberg-Marquardt algorithm for non-linear least squares regression estimation (Marquardt, 1963). All of the fits converged. Goodness of fit was assessed using the root mean squared error (RMSE) and the coefficient of determination (R^2) computed from the observed and predicted values of L for each core. Non-parametric analyses of variance (Kruskal and Wallis, 1952) were performed on the estimated D and c parameters, the RMSE's, and the $\bar{x}$ and τ measurements, to compare median values between the rock groups. Relationships between variables were explored using correlation coefficients (r). Statistical significance was assessed at the $p < 0.05$ level. All of the statistical analyses were performed in the R software environment (R Core Team, 2016).

3.4 Results

Geometric mean aperture widths, $\bar{x}$, ranged from 45 to 190 μm. Their distribution was right skewed, with a median value of 94 μm (Figure 14b). Among rock groups, the Mancos shale (parallel) cores had the largest variability in $\bar{x}$, ranging from 45 to 190 μm. For the Mancos shale (perpendicular) cores, $\bar{x}$ ranged from 64 to 113 μm, while for the Crossville sandstone cores the range was $79 \leq \bar{x} \leq 111$ μm. The median $\bar{x}$ values for the different rock groups were 87, 124, and 93 μm for Mancos shale (parallel), Mancos shale (perpendicular), and Crossville sandstone, respectively; a Kruskal-Wallis test indicated no significant differences between these values.

The fracture tortuosity's, τ, ranged from 1.000 to 1.030, with an overall median value of 1.004. A Kruskal-Wallis test indicated significant differences between the median values of τ for the different rock groups. The Mancos shale (perpendicular) had the highest median τ value (1.008), followed by Mancos shale (parallel) (1.006), and

lastly Crossville sandstone (1.000). The higher τ for Mancos shale (perpendicular) is to be expected since those cores were fractured perpendicular to bedding.

Overall, the fitting of Eq. [3.13] to the experimental L versus t data resulted in excellent correspondence. Typical data sets and fits are shown in Figure 16. The RMSE, which represents the mean distance of observed values from the predicted values, ranged from 0.40 to 1.69 mm (Table 5). Overall, the median RMSE was 0.99 mm. It is not always easy to comprehend the goodness of fit when reported as an RMSE value. Therefore, although not strictly applicable for non-linear regression, we also computed R^2 values for the individual fits. These ranged from 0.789 to 0.993, with a median R^2 of 0.963. Both the RMSE and R^2 values indicate that the proposed model, Eq. [3.13], fitted the observed experimental data very well for the 20 rock cores investigated.

The surface fractal dimension, D, and initial imbibition time, c, parameters estimated by fitting Eq. [3.13] to the experimental L and t values are listed in Table 5. Among all cores, the median D value was 2.24, with individual estimates ranging from 2.04 to 2.45. The median D values for the different rock groups were 2.35, 2.25, and 2.21 for Mancos shale (parallel), Mancos shale (perpendicular), and Crossville sandstone, respectively; there were no significant differences between these values according to a Kruskal-Wallis test. The c parameter provides an estimate of the time at which the water reservoir first contacted the base of the fractured core. The c values ranged from -0.06 to 0.09 s, with a median of 0.02 s. A Kruskal-Wallis test indicated no significant differences in median c values among the rock groups.

3.5 Discussion and Conclusions

The model presented here, Eqs. [3.12] and [3.13], neglects gravity and can only be used to predict early time behavior. To predict the maximum height that a wetting fluid will attain due to spontaneous imbibition within a fracture, further research will be required. Specifically the effect of gravity will need to be incorporated into the theoretical derivation. The current model also assumes the fracture occurs within an

impermeable matrix. This assumption is perfectly reasonable for the low porosity rock types, with matrix permeabilities ranging from 10^{-19} to 10^{-17} m^2 (Mokhtari and Tutuncu, 2015; Gehne and Benson, 2017), investigated in this study. There was no visible evidence of water moving into the matrix over the course of the extremely short (< 2 s) neutron imaging experiments (see Figure 15b). However, the incorporation of a permeable matrix, allowing for spontaneous imbibition of water through the fracture surface, would greatly expand the range of applicability of the proposed model.

At the beginning of the spontaneous imbibition process, liquid velocities are relatively high, resulting in large Reynolds numbers. It has been shown that fracture surface roughness can induce turbulent flow at relatively low Reynolds numbers (Ghezzehei, 2004; Wang et al., 2016). The analytical model we have proposed assumes a laminar flow regime. Therefore, additional investigations are needed to test this assumption and establish critical Reynolds numbers for spontaneous imbibition in rough-walled fractures.

As can be seen in Figure 16, the experimental L versus t data were slightly less variable for Crossville sandstone than for Mancos shale. As a result, individual RMSE values obtained from fitting Eq. [3.13] to the experimental data were generally higher for Mancos shale than for Crossville sandstone (Table 5). The median RMSE for Crossville sandstone was 0.80 mm, as compared to median RMSE's of 1.04 and 0.89 mm for the Mancos shale cores fractured parallel and perpendicular to bedding, respectively. Although not statistically significant (based on a Kruskal-Wallis test), these differences suggest that the model provided a better fit to the sandstone data than to the shale data. This could be due to the presence of more hydrous minerals in the shale samples resulting in darker pixel values during neutron radiography. While the overall trend of wetting could still easily be distinguished in both rock types by change point analysis, the hydrous minerals may have contributed to the variability, and consequently, the higher median RMSE values.

Estimations of the surface fractal dimension, D, ranged from 2.04 to 2.45 (Table 5). All of the estimates fell within the theoretical bounds of $2 \leq D < 3$ for a fractal surface, suggesting that our proposed model is physically sound and that rock fracture surfaces are indeed fractal. Recently, Persson (2014) has argued that, because of the fragility of actual rough surfaces, practical bounds of $2 \leq D < 2.3$ apply to such surfaces. The results in Table 5 indicate that 75% of the estimated D values fell within this restricted range, lending support to his argument.

In the present study the surface fractal dimension, D, was estimated inversely by fitting Eq. [3.13] to experimental wetting height versus time data. However, there is no reason why the fractal model developed here cannot not be used for the forward prediction of water uptake into fractured rocks. To accomplish this D would need to be measured independently in future studies. Babadagli and Develi (2003) have reported estimates of D based on fracture surface roughness measurements with a profilometer. Similar measurements could be made following a spontaneous imbibition experiment. The fractured core would first be oven dried to remove any retained water. It would then be unwrapped and carefully separated along its fracture plane into two halves, each with an exposed fracture surface. Surface profilometry could then be employed to provide an independent estimate of D for forward modeling.

The only significant correlation among the variables was a weak positive relationship between D and $\bar{x}$ ($r = 0.53$, $p < 0.05$). This trend indicates that the fracture aperture width increased as the fracture surface fractal dimension increased. Assuming random roughness, this is to be expected, since the greater the D value, the rougher the fracture surfaces and thus, the greater the separation distance between them.
In conclusion, we have developed an analytical model for spontaneous imbibition of a wetting fluid into a fracture formed by opposing rough fractal surfaces. The model includes a new parsimonious derivation of Hazlett's (1990) equation for the contact angle of a fluid on a rough fractal surface from the well-known Wenzel (1936) equation. The model ignores gravity and is applicable to laminar fluid uptake at early times in

otherwise impermeable rock. The model was tested by fitting it to experimental data for the spontaneous imbibition of deionized water into rock fractures collected using dynamic neutron radiography. Twenty fractured cores from 2 rock types (a tight sandstone and a gas shale) were investigated. Geometric mean aperture widths of the fractures, $\bar{x}$, were measured and entered into the model, while the surface fractal dimension, D, was estimated inversely, along with the initial imbibition time, c. All of the fits successfully converged and there was a close correspondence between the observed and modeled heights of wetting. The estimated D values ranged from 2.04 to 2.45, with a median value of 2.24, which is reasonable for fracture surfaces with fractal roughness.

Chapter 4
A Fractal Model for Spontaneous Imbibition: Further Experimental Validation

4.1 Introduction

In typical porous media, fluid can be transported through interconnected void spaces between grains. Under variably saturated conditions, the phenomenon of spontaneous imbibition drives this process (Kang et al., 2013). Spontaneous imbibition occurs when a wetting fluid enters a porous medium and displaces a present non-wetting fluid. This process is driven by capillary action within interstitial pore spaces (Morrow, 2001; Schmid et al., 2012). Researchers have shown that spontaneous imbibition is much faster within fracture zones than in the surrounding matrix (Hall, 2013; Cheng et al., 2015; Tokunaga and Wan, 2001; Şahmaran et al., 2009) (refer to Figure 1). In low-porosity rocks, where matrix imbibition is minimal, fracture imbibition is likely to play a greater role in fluid transport relative to matrix imbibition (Cheng et al., 2015). Several industries such as Carbon Sequestration and Deep Waste Storage rely on low-porosity rocks to inhibit fluid flow. However, these low-porosity rocks, when fractured, contain conduits where spontaneous imbibition can drive fluid uptake. Other industries such as construction, often use low-porosity rocks such as granite and limestone as building materials. These materials, if fractured, can deteriorate with time due to repeated wetting within the fracture zone from spontaneous imbibition. Thus, it is important to understand how low porosity rock types typically used in these industries respond to spontaneous imbibition within fracture zones.

4.1.1 Carbon Capture and Storage

In an initiative to lower global carbon emissions, Carbon Capture and Storage technology has been widely considered as a potential solution as seen in places such as Sleipner, Norway and Weyburn, Canada (Intergovernmental Panel on Climate Change, 2005). Carbon capture and storage typically involves the capture of CO_2 generated from

industrial processes, the compression of the CO_2 into a dense fluid state, and then subsequent injection of that captured CO_2 into underground rock formations deemed suitable for sequestration (Gaurina-Međimurec et al., 2017; Intergovernmental Panel on Climate Change, 2005). These formations are generally quite porous, and often either hold fluids (e.g. brines, oil, natural gas), or have previously held fluids. To ensure proper sequestration of the injected CO_2, and to limit potential migration, CO_2 is injected into formations upon which a low porosity, low permeability unfractured caprock overlies the storage formation (Intergovernmental Panel on Climate Change, 2005).

A high seal potential of the overlying caprock is integral in successful carbon storage. This seal potential is often evaluated based on the integrity of the caprock as well as the sealing capacity. The integrity of the caprock is considered based on the presence of fracture systems and faults and their ability to aid in migration of CO_2 (Gaurina-Međimurec et al., 2017). The seal capacity of the caprock is determined by the amount of CO_2 underlying the caprock that can be retained without allowing for capillary entry into the seal (Jimenez and Chalaturnyk, 2002; Kaldi et al., 2013).

Jimenez and Chalturnyk (2002) suggest that tight granular rocks such as granites, have the potential to hold very large columns of CO_2, thus having a high seal capacity. This high seal capacity suggests that capillary leakage is likely to be minimal in these rock types. However, while some porous media may show a slower rate of imbibition within its respective matrix, rapid imbibition can occur within in situ fractures (Cheng et al., 2015; Hall, 2013). Thus, it is important to understand how potential caprocks could potentially leak due to rapid imbibition of fluids within fractured zones.

4.1.2 Nuclear and Chemical Deep Waste Repositories

Long-lived hazardous nuclear and chemical wastes require a cost effective form of disposal that has a low environmental and health impact. Many disposal ideas abound such as deep-seabed disposal, disposal in polar ice sheets, and rocketing waste into space (Kim et al., 2011). However, deep geological waste repositories in low-

porosity rocks (e.g. granites, salt, and clays) are often considered as a practical solution (Falck and Nilsson, 2009).

For high-level nuclear and chemical wastes, a combination of low-porosity rocks and engineered materials are used for deep storage (Suzuki et al., 2018). Rather than storing waste in porous rock formations as done with CO_2, these wastes are encapsulated in an engineered canister and then placed in a shaft within a host rock, typically a granite. A bentonite clay buffer is placed around the canister and is then overlain by a back-fill of clay and host rock material. Lastly, a concrete plug is used to seal the entire storage location (Suzuki et al., 2018; Kim et al., 2011; Falck and Nilsson, 2009). Fractures created during excavation as well as the presence of pre-existing natural fractures may provide potential migration pathways for leaking waste.

4.1.3 Deterioration of Engineered Structures

Spontaneous imbibition research for porous media has generally focused on building materials such as mortar, masonry brick, and dry concrete using the rate of imbibition as a measure of potential material durability (Lockington and Parlange, 2003). These studies imply that a decreased rate of imbibition indicates the likelihood of a material to resist exposure to fluids and reactive solutes (Lockington and Parlange, 2003). Thus, a faster imbibition rate allows for increased exposure to fluids promoting material deterioration. Researchers have shown that increased imbibition occurs within fractures and can cause degradation of building materials by repeated wetting within microcracks (Bao et al., 2017; Şahmaran et al., 2009). As these building materials are rarely fully saturated, spontaneous imbibition is a likely process driving water movement within the fractures. Further research is needed to better understand the response of common low-porosity building materials, such as granite and limestone, to fracture spontaneous imbibition. This can help to inform material selection in the construction process as well as determine a given material's durability and integrity.

The objective of this chapter, is to further test the analytical model developed in chapter 3 for spontaneous imbibition within a fracture bounded by parallel rough fractal

surfaces, using potential caprock, host rock, and building materials. The model will be tested by fitting it to experimental data for the spontaneous imbibition of water into air-filled fractured rock cores collected using neutron radiography.

4.3 Materials and Methods

To apply the fractal model derived in chapter 3 to low porosity rock types typical of those used for caprocks, deep waste storage, and building materials, similar methods were employed as outlined in the methods section of chapter 3.

Four rock types were investigated: a low porosity limestone (Burlington Limestone) and three granites (Sierra White, Vermilion Bay Granite, and Westerly). Similar to previous chapters, core samples (5.08 cm long × 2.54 cm diameter) of each rock type were obtained from Kocurek Industries Inc. (Caldwell, TX, USA). The samples were cored from surface outcrops with unknown locations. See section 2.2.1 and Table 1 for detailed background information on these rock types.

As outlined in chapter 3, each rock core was wrapped in Kapton® tape and fractured using the Brazilian method (Li and Wong, 2013; Cheng et al., 2015). The fracture width was then measured at 20 locations on both ends of each core, resulting in 40 measurements per core. The resulting data (not shown) were log-normally distributed, and geometric mean aperture widths, $\bar{x}$, were calculated from these measurements. All cores were then oven dried to a zero initial moisture content and immediately placed into a humidity controlled container to prevent changes in the core's moisture content prior to placement in the neutron beam. See section 3.3 methods for more details on the core preparation.

Dynamic neutron radiography was employed to measure the spontaneous imbibition of water within the fractured rock cores. The imaging was performed at Oak Ridge National Laboratory's Neutron Imaging Facility (beam line CG-1D, HFIR). The configuration and specifications of this cold neutron beam line are described in Santodonato et al. (2015). Neutron radiographs were obtained using the sCMOS

detector at a rate of 30 frames per second. The field of view was 28 mm x 28 mm, and the spatial resolution was 100 μm. Cores were placed individually in front of the sCMOS detector with their fracture planes oriented parallel to the neutron beam. Each core was imaged as it was brought into contact with a deionized-water reservoir following Cheng et al. (2015) (refer to Figure 15a). The resulting uptake of water within the fracture was imaged as a series of time-stamped neutron radiographs.

The radiographs were normalized to ensure visualization of the water (shown as black pixels). To do this, dark-field images were subtracted from radiographs captured both prior to and during wetting. The resulting wetting images were then divided by one of the dry images yielding the final normalized radiographs for each core (refer to Figure 15b). For each time series of normalized radiographs, a 50 pixel wide transect was superimposed over the fracture from the base of the core to the top of the image. The fracture transect was segmented so as to closely follow any deviations from linearity in the fracture. The total length of the transect, L_T, was then used to compute the fracture tortuosity, τ, using the relationship $\tau = \frac{L_T}{L_S}$, where L_S is the straight line distance between the two ends of the transect.

Pixel gray-scale values were averaged over the width of each superimposed transect, resulting in an average gray-scale value for each pixel length of the transect (refer to Figure 15c). Change point analysis, as described by Eckley et al. (2011), was employed to determine L in Eq. [4.1] by detecting the distance the water had moved along the transect in each normalized neutron radiograph. The change points were converted from pixel values to millimeters by comparing the measured diameter of the core in the radiograph to its known diameter. Corresponding t values in Eq. [4.1] were extracted from the radiograph time stamps.

Between 13 and 80 pairs of L and t values were collected for each core (see Table 6). The surface fractal dimension, D, and initial imbibition time, c, were estimated by fitting Eq. [4.1] to the experimental L and t values on a core-by-core basis using the Levenberg-Marquardt algorithm for non-linear least squares regression estimation

(Marquardt, 1963). Physico-chemical constants including absolute viscosity (8.9×10^{-5} dyn·s·mm^{-2}) and surface tension of the liquid-vapor interface (7.2 dyn·mm^{-1}) for water at 25°C were specified in the model (CRC Handbook of Chemistry and Physics, 2018). All other measured parameters were also specified. All of the fits converged. Goodness of fit was assessed using the root mean squared error (RMSE) and the coefficient of determination (R^2) computed from the observed and predicted values of L for each core. Non-parametric analyses of variance (Kruskal and Wallis, 1952) were performed on the estimated D and c parameters, and the RMSE values to compare median values between the rock groups. A non-parametric analysis of variance was also performed on the geometric mean aperture widths to test for any differences among rock types. Relationships between variables were explored using correlation coefficients (r). Statistical significance was assessed at the $p < 0.05$ level. All of the statistical analyses were performed in the R software environment (R Core Team, 2016).

4.2 Model Review

In chapter 3, an analytical model for spontaneous imbibition within a fracture bounded by parallel rough fractal surfaces was developed (refer to Eq. [3.13]) now shown here as Eq. [4.1].

$$L \approx \left(\frac{\bar{x}\gamma}{3\mu\ell^{2-D}}\right)^{\frac{1}{D}} (t-c)^{\frac{1}{D}} \qquad [4.1]$$

In Eq. [4.1], the height of wetting L at any given time t in a sequence of measurements is determined experimentally. Unknown parameters, to be estimated by fitting Eq. [4.1] to the experimental L versus t data, are D and c, where D is the surface fractal dimension and c is a constant introduced as the initial imbibition time. The other parameters in Eq. [4.1], γ, μ, $\bar{x}$ and ℓ, are all known quantities; γ and μ are physico-chemical constants of surface tension and absolute viscosity whose values are available in tables, $\bar{x}$ can be measured by image analysis (see Materials and Methods), and the lower length limit of fractal scaling, ℓ, is taken to be the length of the ruler used for the experimental measurements, i.e. pixel length in neutron radiography.

4.4 Results

Among rock types, geometric mean aperture widths, $\bar{x}$, ranged from 108 to 259 μm with a median of 164 μm (see Figure 17). Their distribution was right skewed. The Burlington Limestone cores had the largest variability in geometric mean aperture width ranging from 113 to 244 μm. For the Sierra White Granite cores, $\bar{x}$ ranged from 115 to 232 μm, while for the Vermilion Bay Granite B cores $108 \leq \bar{x} \leq 180$ μm. The Westerly Granite cores ranged in $\bar{x}$ from 218 to 259 μm. The median $\bar{x}$ values for the different rock groups were 176, 231, 125, and 239 μm for Burlington Limestone, Sierra White Granite, Vermilion Bay Granite B, and Westerly Granite, respectively; a Kruskal-Wallis test indicated significant differences between the rock types at $p < 0.05$.

The fracture tortuosity's, τ, ranged from 1.000 to 1.036, with an overall median value of 1.006. A Kruskal-Wallis test indicated no significant differences between the median values of τ for the different rock groups at $p < 0.05$. The Vermilion Bay Granite B had the highest median τ value (1.015), followed by Westerly Granite (1.006) and the Burlington Limestone (1.004). Lastly, Sierra White Granite had the lowest median τ value (1.003).

The fitting of Eq. [4.1] to the experimental L versus t data resulted in excellent correspondence. Typical data sets and fits are shown in Figure 18. RMSE, which represents the mean distance of observed values from the predicted values, ranged from 0.52 to 2.58 mm (see Table 6). Overall, the median RMSE was 1.40 mm. R^2 values between observed and predicted values were also computed for the individual fits. These ranged from 0.706 to 0.993, with a median R^2 of 0.931. The Burlington Limestone had the greatest variability in R^2, with values ranging from 0.706 to 0.993. The Sierra White Granite seems to have given the most consistent fitting with R^2 ranging from 0.979 to 0.988. Both the RMSE and R^2 values indicate that the proposed model, Eq. [4.1], fitted the observed experimental data very well for the 24 rock cores investigated.

The surface fractal dimension, D, and initial imbibition time, c, parameters estimated by fitting Eq. [4.1] to the experimental L and t values are listed in Table 6.

Among all cores, the median D value was 2.31, with individual estimates ranging from 2.11 to 2.53. The median D values for the different rock groups were 2.24, 2.28, 2.33 and 2.35 for Burlington Limestone, Sierra White Granite, Vermilion Bay Granite B, and Westerly Granite, respectively; there were no significant differences between these values according to a Kruskal-Wallis test at $p < 0.05$. Among all cores, the lowest D value representing the lower bounds of the calculated 95% confidence interval was 2.10. The highest D value representing the upper bounds of the calculated 95% confidence interval was 2.54. The c parameter provides an estimate of the time at which the water reservoir first contacted the base of the fractured core. The c values ranged from -0.03 to 0.03 s, with a median of 0.02 s. A Kruskal-Wallis test indicated no significant differences in median c values among the rock groups. Using correlation coefficients (r), no statistical relationships were found between variables at the $p < 0.05$ level.

4.5 Discussion and Conclusions

The spontaneous imbibition model fit the experimental data very well, converging in all cases. RMSE values obtained by fitting Eq. [4.1] to experimental L and t values indicate that the model fit the experimental data for several rock types very closely (see Figure 18). While not significantly different in RMSE values among rock types (based on a Kruskal-Wallis test), the model seemed to most closely fit the Sierra White Granite data, with RMSE values ranging from 0.59 to 0.74 mm and a median value of 0.71 mm. The model also showed exceptional fits on the other rock types as seen in Figure 18, with median RMSE values of 2.32, 1.40, and 1.23 mm for Burlington Limestone, Vermilion Bay Granite B, and Westerly Granite, respectively. Estimated surface fractal dimensions, D, for all of the rock cores fell within the theoretical bounds of $2 \leq D < 3$ for a fractal surface, suggesting that the proposed model is physically sound and that rock fracture surfaces are indeed fractal.

Future research should focus on forward prediction using the proposed model as a method in evaluating capillary leakage of caprocks and host rocks through in situ

fractures. This could be done by measuring the fractal dimension, D, for fracture surfaces in the desired caprock, by using a an instrument such as a profilometer (Babadagli and Develi, 2003). With D as a known parameter, as well as probable measurements for other known parameters, γ, μ, $\bar{x}$ and ℓ, spontaneous imbibition within a fractured low porosity caprock could be predicted.

In this study, deionized water displacing air at atmospheric pressure was used for all of the spontaneous imbibition measurements. However, other wetting (e.g. brine) and non-wetting (e.g. CO_2 in a dense fluid state, methane, and oil) fluids, should theoretically work with this model as long as model parameters such as the fluid viscosity and surface tension are known. Future research should focus on testing this model with other fluids such as those mentioned above, and possibly at pressures relevant to deep subsurface conditions.

In conclusion, a theoretical model for spontaneous imbibition within fractures with parallel fractal surfaces was tested on caprock materials potentially usable for carbon sequestration, waste storage repositories, and building stone. The model successfully estimated the fractal dimensions within expected theoretical bounds of the rock types tested. The model was tested by fitting it to experimental data for the spontaneous imbibition of deionized water into rock fractures collected using dynamic neutron radiography. Twenty four fractured cores from 4 rock types (a low porosity limestone and three granites) were investigated. Geometric mean aperture widths of the fractures, $\bar{x}$, were measured and entered into the model, while the surface fractal dimension, D, was estimated inversely, along with the initial imbibition time, c. All of the fits successfully converged and there was a close correspondence between the observed and modeled heights of wetting. The estimated D values ranged from to 2.11 to 2.53 with a median value of 2.31, which is reasonable for fracture surfaces with fractal roughness.

Chapter 5
Conclusions and Suggestions for Future Research

5.1 Conclusions

The overall goal of this study was to both measure and model spontaneous imbibition within unsaturated, fractured low-porosity rocks in order to better understand their hydraulic properties. Eight rock types were analyzed including: Burlington Limestone, Crossville Sandstone, Mancos Shale (core both perpendicular and parallel to bedding planes), Sierra White Granite, Vermilion Bay Granites (two varieties), and Westerly Granite (refer to Table 1). These rocks were chosen as they represent examples of low-porosity rock types used in various industrial applications. These applications include oil and gas recovery, hydraulic fracturing, deep waste storage, and the building of engineered structures. Thus, knowing their hydraulic properties with regard to spontaneous imbibition can be of benefit to society.

Spontaneous imbibition of water was visualized and measured on a total of 43 rock cores of length 5.08 cm and a diameter of 2.54 cm representing several replicates of each of the eight rock types. These cores were fractured between flat parallel plates using the Brazilian method. In order to assess the influence of aperture width on spontaneous imbibition within fracture zones, each rock type was characterized by the geometric mean aperture width. In general, the igneous rocks tended to have larger aperture widths while sedimentary rocks had smaller aperture widths. Fractures among the different rock types ranged in geometric mean aperture widths from 84 to 205 μm (refer to Table 2). The fracture widths were significantly correlated with both solid phase density and porosity. While not the focus of this study, the solid phase density had the strongest correlation with fracture width ($r = 0.92$, $p < 0.05$) indicating that mechanical properties related to the mineralogy of the individual cores likely plays a large role in determining the width of apertures produced by the Brazilian method.

Spontaneous imbibition of water displacing air was visualized within the fracture zone of each of the eight rock types. This was done by implementing dynamic neutron

radiography to image the movement of water within the fractures of the 43 cores. Neutron radiographs were generated during this process, allowing for the quantitative measurement and modeling of spontaneous imbibition within the rock core fracture zone. The wetting fronts portrayed a square-root of time behavior, allowing fracture sorptivity values to be computed. Fracture sorptivity values ranged from 13.2 to 33.7 $mm \cdot s^{-0.5}$. The fracture sorptivity parameter differed among rock types, with sedimentary cores generally resulting in larger values relative to igneous cores. A significant negative correlation between fracture sorptivity and Wenzel roughness factor was found, indicating that fracture sorptivity tends to decrease as fracture surface roughness increases among these rock types.

A theoretical model for spontaneous imbibition within a fracture comprised of parallel fractal surfaces was derived and tested on gas shale's and tight gas sandstones (e.g. Mancos Shale and Crossville Sandstone), as well as rock types similar to caprocks in deep waste repositories (e.g. Sierra White Granite, Vermilion Bay Granite, and Westerly Granite). A low porosity limestone sample (Burlington Limestone) relevant to building materials was also tested. In total, the model was validated using 44 cores, which were different from those measured in Chapter 2 (i.e. no duplicate cores were used). Of these cores, several replicates of the different rock types were tested (refer to Tables 5 and 6). Similar to the samples used for the measurement of spontaneous imbibition, these rock cores were fractured using the Brazilian method, inducing a planar mode-I fracture. Among these 44 cores, median fracture aperture widths and fracture tortuosities were significantly different between the different rock types (see Table 7). The theoretical model was fitted to experimental fracture imbibition data obtained through dynamic neutron radiography. All of the fits converged for the 44 rock cores investigated (i.e. cores analyzed in Chapters 3 and 4). Surface fractal dimensions, D, were estimated inversely and ranged from 2.04 to 2.53. All 44 estimates were within the theoretical bounds for a rough fractal surface, i.e. $2 \leq D < 3$, although there were no significant differences between the median D values for the different rock types (see Table 7). This

proposed theoretical model may be a suitable way to estimate fracture surface roughness based upon spontaneous imbibition data for fractured low porosity rocks.

Among the cores analyzed in Chapters 3 and 4, a weak positive correlation was found between D and the geometric mean aperture width, $\bar{x}$ (r = 0.34, $p < 0.05$, DF = 42). No other significant correlations were found between the model variables D and $\bar{x}$, and other measured values (i.e. contact angle, porosity, solid phase density, sorptivity, tortuosity, and Wenzel roughness).

Measurements of the geometric mean aperture widths in Chapter 2 and those measured in Chapters 3 and 4 were quite similar. The Westerly Granite produced the largest geometric mean aperture width in both experiments. The Mancos Shale and Crossville Sandstone yielded the smallest apertures. A strong positive correlation (r = 0.91, $p < 0.05$) existed between the geometric mean aperture widths measured in Chapter 2 and those reported in Chapters 3 and 4, indicating that despite some variation, the aperture widths were consistent in both experiments.

5.2 Suggestions for Further Research

This study provided measurements of spontaneous imbibition within unsaturated, fractured low-porosity rocks. If possible, future investigations of the influence of fracture surface roughness on the rate of fracture spontaneous imbibition should implemented using larger core sizes. In this study, relatively small cores (25.4 mm in diameter by 50.8mm in length) were used. However, as suggested by Vogler et al. (2017), small core sizes may produce rougher surfaces from intragranular fractures. The use of larger core sizes would allow for the production of more natural fractures along grain boundaries when using the Brazilian method for fracturing. Thus, a more realistic fracture and fracture roughness would be produced allowing for a more realistic simulation of natural in situ fracture imbibition.

During the fracturing process of this study, it was noted that, qualitatively, certain rock types possessed varying tensile strengths, thus resulting in higher or lower

loading stresses to induce failure. Specific measurements of the stress applied at failure would allow for increased rock type characterization as well as potentially provide a quantifiable measurement of fracture variability within similar rock types.

A theoretical model for spontaneous imbibition within the fracture zone was developed. This model, however, has a few assumptions which could be improved upon in future studies. The current model ignores gravity and focuses on early time imbibition. With a focus on early time imbibition, the model does not account for lateral movement of water into pore spaces; the model assumes an impermeable matrix. This assumption is perfectly reasonable for the low porosity rock types investigated in this study, specifically during early time imbibition. There was no visible evidence of water moving into the matrix over the course of the extremely short (< 2 s) neutron imaging experiments (see Figure 15b). However, the incorporation of a permeable matrix, allowing for spontaneous imbibition of water through the fracture surface, would greatly expand the range of applicability of the proposed model and better represent late time imbibition. Thus, further work should focus on the inclusion of gravity (i.e. extending the model to late time) as well as accounting for a permeable matrix.

The present model also assumes a laminar flow regime during fracture imbibition. However, at the beginning of the spontaneous imbibition process, liquid velocities are relatively high, resulting in large Reynolds numbers. It has been shown that fracture surface roughness can induce turbulent flow at relatively low Reynolds numbers (Ghezzehei, 2004; Wang et al., 2016). Therefore, additional investigations are needed to test this assumption and establish critical Reynolds numbers for spontaneous imbibition in rough-walled fractures. Finally, spontaneous imbibition within the fracture zone was measured solely at a zero-gauge pressure. Further research and incorporation of confining pressures into the spontaneous imbibition model could be beneficial.

Lastly, future studies should focus on the forward prediction of spontaneous imbibition using the derived spontaneous imbibition model. This could be done using independent estimates of the fractal dimension obtained from surface roughness data measured for example using a profilometer, as was accomplished by Babadagli and Develi (2003). These independent measurements could then be used in the model to forwardly predict spontaneous imbibition for a given material and fluid.

References

Alfarge, D., M. Wei, and B. Bai. 2017. IOR methods in unconventional reservoirs of North America: comprehensive review. Soc. Petrol. Eng. doi:10.2118/185640-MS

Babadagli, T. 2005. Analysis of oil recovery by spontaneous imbibition of surfactant solution. Oil Gas Sci. Technol. – Rev. IFP, 60: 697-710

Babadagli, T., and K. Develi. 2003. Fractal characteristics of rocks fractured under tension. Theor. Appl. Fract. Mech. 39: 73–88

Bao, J. W., and L. C. Wang. 2017. Capillary imbibition of water in discrete planar cracks. Construction and Building Materials, 146, 381-392. doi: 10.1016/j.conbuildmat.2017.04.129

Beaulieu, C., J. Chen, and J.L. Sarmiento. 2012. Change-point analysis as a tool to detect abrupt climate variations: Phil Trans. Royal Soc. A. 370: 1228-1249

Boffa, J.M., C. Allain, and J.P Hulin. 1998. Experimental analysis of fracture rugosity in granular and compact rocks. Eur. Phys. J. AP 2: 281-289

Brace, W. F., J. B. Walsh, and W. T. Frangos. 1968. Permeability of granite under high pressure. Journal of Geophysical Research, 73(6), 2225-2236. doi: 10.1029/JB073i006p02225

Brown, S. R. 1987. Fluid flow through rock joints: The effect of surface roughness. Journal of Geophysical Research: Solid Earth, 92(B2), 1337-1347. doi: doi:10.1029/JB092iB02p01337

Cai, J., B.-M. Yu, M.-F. Mei, and L. Luo. 2010. Capillary rise in a single tortuous capillary. Chinese Phys. Lett. 27, 054701

Cheng, C. L., E. Perfect, B. Donnelly, H.Z. Bilheux, A.S. Tremsin, L.D. McKay, V.H. DiStefano, J.-C. Cai, and L.J. Santodonato. 2015 Rapid imbibition of water in fractures within unsaturated sedimentary rock. Adv. Water Resour. 77: 82-89

Cheng, Yueming. 2012. Impact of Water Dynamics in Fractures on the Performance of Hydraulically Fractured Wells in Gas-Shale Reservoirs. doi: 10.2118/127863-PA

CRC Handbook of Chemistry and Physics. 2018. CRC Press/Taylor and Francis, Boca Raton, FL, ISBN 9781498784542

Cui, C.J., M.W Mozur, U.E Verre, and F.N Weltge. 2014. Unconventional and conventional hydrocarbon resource economics: a look at the fundamental differences and how countries can address the needs of unconventional resource exploitation. Soc. Petrol. Eng. doi:10.2118/169873-MS

Culligan, P. J., V. Ivanov, and J.T. Germaine. 2005. Sorptivity and liquid infiltration into dry soil: Advances in Water Resources. v. 28, no. 10, p. 1010-1020

Dehghanpour, H., Q, Lan, Y. Saeed, H. Fei, and Z. Qi. 2013. Spontaneous imbibition of brine and oil in gas shales: effect of water adsorption and resulting microfractures. Energy Fuels 27: 3039–3049

Develi, K., and T. Babadagli. 1998. Quantification of natural fracture surfaces using fractal geometry. Math. Geol. 30: 971-998

Donnelly, B., E. Perfect, L.D. McKay, P.J. Lemiszki, V.H. DiStefano, L.M. Anovitz, J. McFarlane, R.E. Hale, and C.–L. Cheng. 2016. Capillary pressure – saturation relationships for gas shales measured using a water activity meter. J. Natural Gas Sci. 33: 1342-1352

Eckley, I.A., P. Fearnhead, and R. Killick. 2011. Analysis of changepoint models, p. 205-224 In D. Barber, A.T Cemgil, and S. Chiappa (eds.), Bayesian Time Series Models, Cambridge University Press, Cambridge, UK, 432 pp.

Erdman, C. and J.W. Emerson. 2008. A fast bayesian change point analysis for the segmentation of microarray data. Bioinformatics. 24: 2143–2148

Falck, W., and K.-F. Nilsson. 2009. Geological Disposal of Radioactive Waste: Moving Towards Implementation. Joint Research Centre. doi: 10.2790/12387

Fernø, M.A. 2012. Enhanced oil recovery in fractured reservoirs, p. 89-110 In: L. Romero-Zerón (Ed.), Introduction to enhanced oil recovery (EOR) processes and bioremediation of oil-contaminated sites, InTech, ISBN: 978-953-51-0629-6

Gates, C.H. 2018. Estimating wettability of rock fracture surfaces from contact angle and roughness measurements. M.S. Thesis, Department of Earth and Planetary Sciences, University of Tennessee, Knoxville, TN

Gaurina-Međimurec , N., and K. N. Mavar. 2017. Depleted hydrocarbon reservoirs and CO2 injection wells - CO2 leakage assessment. Rudarsko-Geolosko-Naftni Zbornik, 32(2), 15-27. doi: 10.17794/rgn.2017.2.3

Gehne, S., and P.M. Benson. 2017. Permeability and permeability anisotropy in Crab Orchard sandstone: experimental insights into spatio-temporal effects. Tectonophysics 712/ 713: 589-599

Ghanbari, E., and H. Dehghanpour. 2016. The fate of fracturing water: A field and simulation study. Fuel, 163, 282-294. doi: https://doi.org/10.1016/j.fuel.2015.09.040

Ghezzehei, T A. 2004. Constraints for flow regimes on smooth fracture surfaces. Water Resour. Res., 40, W11503, doi:10.1029/2004WR003164

Hall, C. 1989. Water Sorptivity of Mortars and Concretes – a review. Magazine of Concrete Research, 41(147), 51-61.

Hall, S. A. 2013. Characterization of fluid flow in a shear band in porous rock using neutron radiography. Geophysical Research Letters, 40(11), 2613-2618. doi: 10.1002/grl.50528

Hanzic, L., and R. Ilic. 2003. Relationship between liquid sorptivity and capillarity in concrete. Cement and Concrete Research, 33(9), 1385-1388. doi: 10.1016/s0008-8846(03)00070-x

Hazlett, R.D. 1990. Fractal applications: wettability and contact angle. J. Colloid Interface Sci. 137: 527-533

Huang, N., R. C. Liu, and Y. J. Jiang. 2017. Numerical study of the geometrical and hydraulic characteristics of 3D self-affine rough fractures during shear. Journal of Natural Gas Science and Engineering, 45, 127-142. doi: 10.1016/j.jngse.2017.05.018

Huang, N., R. C. Liu, Y.Y Jiang, B. Li, and L.Y. Yu. 2018. Effects of fracture surface roughness and shear displacement on geometrical and hydraulic properties of

three-dimensional crossed rock fracture models. Advances in Water Resources, 113, 30-41. doi: 10.1016/j.advwatres.2018.01.005

Intergovernmental Panel on Climate Change. 2005. IPCC Special Report on Carbon Dioxide Capture and Storage. In B. D. Metz, O. Coninck, H. Loos, M. Meyer, L. (Ed.), (pp. 442). New York, USA.

Javaheri, A., H. Dehghanpour, and J. Wood. 2017. Imbibition oil recovery from tight rocks with dual-wettability pore-network A Montney case study. Soc. Petrol. Eng. doi:10.2118/185076-MS

Jiang, Yun, Shi, Yang, Xu, Guoqing, Jia, Chen, Meng, Zhan, Yang, Xianyou, . . . Ding, Bin. 2018. Experimental Study on Spontaneous Imbibition under Confining Pressure in Tight Sandstone Cores Based on Low-Field Nuclear Magnetic Resonance Measurements. Energy and Fuels, 32(3), 3152-3162. doi: 10.1021/acs.energyfuels.7b03776

Jennings, C.W., R.G. Strand, and T.H. Rogers. 1977. Geologic map of California. Retrieved from https://mrdata.usgs.gov/geology/state/sgmc-unit.php?unit=CAgrMZ3;0

Jimenez, J. A., and R. J. Chalaturnyk. 2002. Integrity of Bounding Seals for Geological Storage of Greenhouse Gases. Paper presented at the SPE/ISRM Rock Mechanics Conference, Irving, Texas

Kaldi, J., R. Daniel, E. Tenthorey, K. Michael, U. Schacht, A. Nicol, J. Underschultz, and G. Backé. 2013. Containment of CO2 in CCS: Role of caprocks and faults (Vol. 37).

Kanematsu, M., I. Maruyama, T. Noguchi, H. Iikura, and N. Tsuchiya. 2009. Quantification of water penetration into concrete through cracks by neutron radiography. Nuclear Instruments and Methods in Physics Research Section A: Accelerators, Spectrometers, Detectors and Associated Equipment, 605(1), 154-158. doi: https://doi.org/10.1016/j.nima.2009.01.206

Kang, M., E. Perfect, C. -L. Cheng, H.Z. Bilheux, M. Gragg, D.M. Wright, J.M. Lamaana, J. Horita, and J.M. Warren. 2013. Diffusivity and Sorptivity of Berea Sandstone

Determined using Neutron Radiography. Vadose Zone Journal, 12(3). doi: 10.2136/vzj2012.0135

Karpyn, Z. T., P.M. Halleck, and A.S. Grader. 2009. An experimental study of spontaneous imbibition in fractured sandstone with contrasting sedimentary layers. Journal of Petroleum Science and Engineering, 67(1), 48-56. doi: https://doi.org/10.1016/j.petrol.2009.02.014

Keller, A. 1998. High resolution, non-destructive measurement and characterization of fracture apertures. Int. J. Rock Mech. Min. Sci. 35: 1037-1050

Kim, J.-S., S. –K. Kwon, M. Sanchez, and G. –C. Cho. 2011. Geological storage of high level nuclear waste. KSCE Journal of Civil Engineering, 15(4), 721-737. doi: 10.1007/s12205-011-0012-8

King, G.E. 2012. Hydraulic Fracturing 101: What Every Representative, Environmentalist, Regulator, Reporter, Investor, University Researcher, Neighbor and Engineer Should Know About Estimating Frac Risk and Improving Frac Performance in Unconventional Gas and Oil Wells. Paper presented at the SPE Hydraulic Fracturing Technology Conference, The Woodlands, Texas, USA

Konzuk, J.S., and B.H. Kueper. 2004. Evaluation of cubic law based models describing single-phase flow through a rough-walled fracture. Water Resour. Res. 40, W02402, doi:10.1029/2003WR002356

Koyama, T., B. Li, Y. Jiang, and L. Jing. 2008. Numerical simulations for the effects of normal loading on particle transport in rock fractures during shear. International Journal of Rock Mechanics and Mining Sciences, 45(8), 1403-1419. doi: 10.1016/j.ijrmms.2008.01.018

Kruskal, W.H., and W.A. Wallis. 1952. Use of ranks in one-criterion variance analysis. J. Am. Stat. Assoc. 47: 583–621

Li, D. Y., and L.N.Y. Wong. 2013. The Brazilian disc test for rock mechanics applications: review and new insights. Rock Mech. Rock Eng. 46: 269-287

Li, Q., H. Xing, J. Liu, and X. Liu. 2015. A review on hydraulic fracturing of unconventional reservoir. Petroleum 1: 8-15

Lockington, D. A., and J.Y. Parlange. 2003. Anomalous water absorption in porous materials. Journal of Physics D-Applied Physics, 36(6), 760-767. doi: 10.1088/0022-3727/36/6/320

Mandelbrot, B.B., 1982. The fractal geometry of nature. W. H. Freeman and Company, New York, NY, USA, 468 pp.

Marquardt, D. 1963. An algorithm for least-squares estimation of nonlinear parameters. J. Soc. Indust. Appl. Math. 11: 431-441

Mason, G., and N.R. Morrow. 2013. Developments in spontaneous imbibition and possibilities for future work. J. Petrol. Sci. Eng. 110: 268-293

Meng, Q., H. Liu, and J. Wang. 2017. A critical review on fundamental mechanisms of spontaneous imbibition and the impact of boundary condition, fluid viscosity and wettability. Adv. Geo-Energ. Res. 1: 1-17

McLennan, J.D., J.C. Roegiers, and W.P. Marx. 1983. The Mancos formation: an evaluation of the Interaction of geological conditions, treatment characteristics and production. Soc. Petrol. Eng. doi:10.2118/11606-M

Mokhtari, M., and A.N. Tutuncu. 2015. Characterization of anisotropy in the permeability of organic-rich shales. J. Petrol. Sci. Eng. 133: 496-506

Morrow, N.R., and G. Mason. 2001. Recovery of oil by spontaneous imbibition. Curr. Opin. Colloid Interface Sci., 6: 321-337

Myers, T. 2012. Potential Contaminant Pathways from Hydraulically Fractured Shale to Aquifers. Ground Water, 50(6), 872-882. doi: 10.1111/j.1745-6584.2012.00933.x

Osiptsov, A.A. 2017. Fluid mechanics of hydraulic fracturing: a review. J. Petrol. Sci. Eng. 156: 513-535

Perfect, E., C.L. Cheng, M. Kang, H.Z. Bilheux, J.M. Lamanna, M.J. Gragg, and D.M. Wright. 2014. Neutron imaging of hydrogen-rich fluids in geomaterials and engineered porous media: A review. Earth Sci. Rev. 129: 120-135

Persson, B.N.J. 2014. On the fractal dimension of rough surfaces. Tribol. Lett. 54: 99–106

Philip, J. R., 1957. The theory of infiltration: 4. Sorptivity and algebraic infiltration equations. Soil Sci, v. 84, no. (3), p. 257-264

Power, W.L., and T.E. Tullis. 1991. Euclidean and fractal models for the description of rock surface roughness. J. Geophys. Res. 96: 415-424

Quinn, A. 1971. Bedrock Geology of Rhode Island. Geological Survey Bulletin.

R Core Team. 2016. R: A language and environment for statistical computing. R Foundation for Statistical Computing, Vienna, Austria, https://www.R-project.org/

Rangel-German, E. R., and A.R. Kovscek. 2002. Experimental and analytical study of multidimensional imbibition in fractured porous media. Journal of Petroleum Science and Engineering, 36(1), 45-60. doi: https://doi.org/10.1016/S0920-4105(02)00250-4

Reeves, J., J. Chen, X.L. Wang, R. Lund, and L. Qi. 2007. A review and comparison of changepoint detection techniques for climate data. J. Appl. Meteorol. Climat. 6: 900–915

Russ, J.C. 1994. Fractal surfaces. Plenum Press, New York, NY, USA, 309 pp.

Şahmaran, Mustafa, and V.C. Li. 2009. Influence of microcracking on water absorption and sorptivity of ECC. Materials and Structures, 42(5), 593-603. doi: 10.1617/s11527-008-9406-6

Santodonato, L., H. Bilheux, B. Bailey, J. Bilheux, P. Nguyen, A. Tremsin, D. Selby, and L. Walker. 2015. The CG-1D neutron imaging beamline at the Oak Ridge National Laboratory High Flux Isotope Reactor. Physics Procedia. 69: 104-108

Schmid, K. S., and S. Geiger. 2012. Universal scaling of spontaneous imbibition for water-wet systems. Water Resources Research, 48. doi: 10.1029/2011wr011566

Schneider, C.A., W.S. Rasband, and K.W. Eliceiri. 2012. NIH Image to ImageJ: 25 years of image analysis. Nature Methods 9: 671-675

Shi, Y., M.R. Yassin, and H. Dehghanpour. 2018. A modified model for spontaneous imbibition of wetting phase into fractal porous media. Colloids and Surfaces a-Physicochemical and Engineering Aspects, 543, 64-75. doi: 10.1016/j.colsurfa.2017.12.052

Schwiebert, M.K., and W.H. Leong. 1996. Underfill flow as viscous flow between parallel plates driven by capillary action. IEEE Trans. Part C 19:133-137

Suzuki, A., S. Fomin, V. Chugunov, and T. Hashida. 2018. Mathematical Modeling of Non-Fickian Diffusional Mass Exchange of Radioactive Contaminants in Geological Disposal Formations. Water, 10(2). doi: 10.3390/w10020123

Taha, M. M. R., A.S. El-Dieb, and N.G. Shrive. 2001. Sorptivity: a reliable measurement for surface absorption of masonry brick units. Materials and Structures, 34(241), 438-445. doi: 10.1007/bf02482291

Tokunaga, T. K., and J. Wan. 2001. Surface-zone flow along unsaturated rock fractures. Water Resources Research, 37(2), 287-296. doi: 10.1029/2000WR900242

Towler, B.F., H.L. Lehr, S.W. Austin, B. Bowthorpe, J.H. Feldman, S.K. Forbis, D. Germack, and M. Firouzi. 2017. Spontaneous imbibition experiments of enhanced oil recovery with surfactants and complex nano-fluids. J Surfact. Deterg. 20: 367-377

Turcotte, D.L. 1997. Fractals and chaos in geology and geophysics. 2nd Ed., Cambridge University Press, New York, NY, USA, 398 pp.

Ulusay, R., and J.A. Hudson. 2007. The Blue Book: The Complete ISRM Suggested Methods for Rock Characterization, Testing and Monitoring: 1974-2006. Turkish National Group. 628 pp

U.S. Energy Information Administration. 2011. Review of emerging resources: U.S. shale gas and shale oil plays. Washington D.C., USA, 105 pp

Vengosh, A., R.B. Jackson, N. Warner, T.H. Darrah, & A. Kondash. 2014. A Critical Review of the Risks to Water Resources from Unconventional Shale Gas Development

and Hydraulic Fracturing in the United States. Environmental Science & Technology, 48(15), 8334-8348. doi: 10.1021/es405118y

Vogler, D., S.D.C. Walsh, P. Bayer, and F. Amann. (2018. Comparison of Surface Properties in Natural and Artificially Generated Fractures in a Crystalline Rock (vol 50, pg 2891, 2017). Rock Mechanics and Rock Engineering, 51(1), 359-359. doi: 10.1007/s00603-017-1361-5

Wang, M., Y.-F. Chen, G.-W. Ma, J.-Q. Zhou, and C.-B. Zhou. 2016. Influence of surface roughness on nonlinear flow behaviors in 3D self-affine rough fractures: Lattice Boltzmann simulations. Adv. Water Resour. 96: 373–388

Wang, J., H. Liu, J. Xia, Y. Liu, C. Hong, Q. Meng, and Y. Gao. 2017. Mechanism simulation of oil displacement by imbibition in fractured reservoirs. Petrol. Explor. Develop. 44: 805–814

Wanless, H.R. 1946. Pennsylvanian geology of a part of the southern Appalachian coal field. Geol. Soc. Am. Memoir 13, 162 pp

Wawersik, W. R., and W.F. Brace. 1971. Post-failure behavior of a granite and diabase. Rock mechanics, 3(2), 61-85. doi: 10.1007/bf01239627

Wenzel, R.N. 1936. Resistance of solid surfaces to wetting by water. Ind. Eng. Chem., 28: 988-994

Xiao, Y., F. Yang, and R. Pitchumani. 2006. A generalized analysis of capillary flows in channels. J. Colloid Interface Sci. 298: 880-888

Zeileis, A., A. Shah, and I. Patnaik. 2010. Testing, monitoring, and dating structural changes in exchange rate regimes. Comput. Stat. Data Anal. 54: 1696–1706

Appendices

Appendix 1 - Tables

Table 1: Physical rock properties of the sample rock types as means of measured values with standard errors shown. Abbreviations of rock types listed below rock name. Note only Mancos Shale (perpendicular) was measured denoted here as simply Mancos Shale.

Rock Type	**Bulk Density ($g\ cm^{-3}$)†**	**Solid Phase Density ($g\ cm^{-3}$)†**	**Porosity (%)†**	**Intrinsic Contact Angle (°)‡**	**Wenzel Roughness Factor ‡**
Burlington Limestone (BL)	2.66 ± <0.01	2.70 ± <0.01	1.77 ± 0.09	76.4 ± 3.3	1.63 ± 0.09
Crossville Sandstone (CS)	2.50 ± 0.01	2.65 ± <0.01	5.85 ± 0.27	42.6 ± 4.3	1.62 ± 0.09
Mancos Shale (MS)	2.50 ± 0.01	2.64 ± 0.01	5.59 ± 0.39	38.4 ± 4.9	1.76 ± 0.09
Sierra White Granite (SW)	2.63 ± <0.01	2.67 ± <0.01	1.49 ±0.13	46.2 ± 2.6	1.84 ± 0.13
Vermilion Bay Granite A (VBA)	2.61 ± <0.01	2.63 ± <0.01	0.69 ± 0.15	58.8 ± 4.1	1.88 ± 0.11
Vermilion Bay Granite B (VBB)	2.62 ± <0.01	2.70 ± <0.01	0.81 ± 0.10	55.9 ± 2.9	1.82 ± 0.16
Westerly Granite (WG)	2.63 ± <0.01	2.65 ± <0.01	0.89 ± 0.10	52.5 ± 2.1	1.70 ± 0.16

† Values measured using the method of Donnelly et al. (2016) by Andrew Vial
‡ Values taken from previous study by Gates (2018)

Table 2: Geometric mean aperture width and Tukey's grouping

Rock Type	Geometric Mean Aperture Width (µm)	Grouping	Cores
Burlington Limestone	191	ab	5
Crossville Sandstone	89	d	6
Mancos Shale (parallel)	85	d	6
Mancos Shale (perpendicular)	84	d	6
Sierra White Granite	176	ab	7
Vermilion Bay Granite A	166	b	5
Vermilion Bay Granite B	125	c	4
Westerly Granite	205	a	4

Table 3: Sorptivity values for samples with clarity in neutron radiographs allowing hand measurements. Goodness of fit shown by coefficient of determination R^2. Grayed out samples were excluded from further analyses as $R^2 < 0.9$

Rock Type	Replicates	R^2	Sorptivity (mm $sec^{-0.5}$)
Burlington Limestone	1	0.9071	27.78
Burlington Limestone	2	0.9817	33.50
Burlington Limestone	3	0.9933	40.50
Burlington Limestone	4	0.9999	32.82
Crossville Sandstone	1	0.8274	25.28
Crossville Sandstone	2	0.9860	21.34
Crossville Sandstone	3	0.9818	26.07
Crossville Sandstone	4	0.9038	24.52
Crossville Sandstone	5	0.9836	25.90
Crossville Sandstone	6	0.9915	25.14
Mancos Shale (parallel)	1	0.9982	38.47
Mancos Shale (parallel)	2	0.9508	29.35
Mancos Shale (parallel)	3	0.9158	25.02
Mancos Shale (perpendicular)	1	0.7268	26.20
Mancos Shale (perpendicular)	2	0.9377	18.41
Mancos Shale (perpendicular)	3	0.9451	24.61
Mancos Shale (perpendicular)	4	0.9248	26.13
Mancos Shale (perpendicular)	5	0.9902	29.17
Sierra White Granite	1	0.8622	14.35
Sierra White Granite	2	0.8770	22.27
Sierra White Granite	3	0.9880	16.61
Sierra White Granite	4	0.9647	19.07
Sierra White Granite	5	0.9818	19.16
Vermilion Bay Granite A	1	0.9614	14.32
Vermilion Bay Granite A	2	0.1758	3.28
Vermilion Bay Granite A	3	0.9824	10.08
Vermilion Bay Granite A	4	0.8802	11.12
Vermilion Bay Granite A	5	0.9924	15.35
Vermilion Bay Granite B	1	0.9583	14.02
Vermilion Bay Granite B	2	0.9964	19.32
Vermilion Bay Granite B	3	0.9956	21.27
Vermilion Bay Granite B	4	0.9469	16.16
Westerly Granite	1	0.9732	31.26
Westerly Granite	2	0.9906	29.02
Westerly Granite	3	0.9483	29.00
Westerly Granite	4	0.8845	17.35

Table 4: Mean sorptivity and Tukey's grouping

Rock Type	Mean Sorptivity (mm $sec^{-0.5}$)	Grouping	Cores
Burlington Limestone	33.7	a	4
Crossville Sandstone	24.6	bc	5
Mancos Shale (parallel)	30.9	ab	3
Mancos Shale (perpendicular)	24.6	abc	4
Sierra White Granite	18.3	cd	3
Vermilion Bay Granite A	13.2	d	3
Vermilion Bay Granite B	17.7	cd	4
Westerly Granite	29.8	ab	3

Table 5: Parameter estimates and associated 95% confidence intervals obtained by fitting Eq. [3.13] to the neutron radiography data for each replicate of each rock group

Rock Type	Replicate number	Number of observations	Surface fractal dimension, D	Initial imbibition time, c (s)	RMSE (mm)
Crossville Sandstone	1	24	2.21 ± 0.01	0.03 ± 0.01	1.03
Crossville Sandstone	2	17	2.18 ± 0.02	0.03 ± 0.01	1.36
Crossville Sandstone	3	34	2.24 ± <0.01	0.09 ± <0.01	0.62
Crossville Sandstone	4	26	2.19 ± <0.01	0.03 ± <0.01	0.52
Crossville Sandstone	5	21	2.04 ± 0.01	0.01 ± <0.01	1.17
Crossville Sandstone	6	24	2.23 ± <0.01	0.06 ± <0.01	0.52
Crossville Sandstone	7	24	2.24 ± 0.01	0.03 ± 0.01	0.80
Mancos Shale (parallel)	1	17	2.24 ± 0.01	0.03 ± <0.01	1.04
Mancos Shale (parallel)	2	58	2.45 ± 0.01	0.00 ± <0.01	0.88
Mancos Shale (parallel)	3	41	2.35 ± 0.01	0.07 ± 0.03	1.43
Mancos Shale (parallel)	4	38	2.42 ± 0.02	0.01 ± 0.04	1.69
Mancos Shale (parallel)	5	16	2.08 ± 0.02	-0.01 ± 0.02	0.95
Mancos Shale (parallel)	6	24	2.17 ± 0.01	0.01 ± 0.01	0.56
Mancos Shale (parallel)	7	46	2.37 ± 0.01	0.02 ± 0.03	1.04
Mancos Shale (perpendicular)	1	23	2.26 ± 0.01	0.01 ± <0.01	0.65
Mancos Shale (perpendicular)	2	60	2.33 ± 0.01	-0.01 ± 0.04	1.04
Mancos Shale (perpendicular)	3	62	2.29 ± 0.01	-0.06 ± 0.03	1.51
Mancos Shale (perpendicular)	4	25	2.25 ± 0.02	-0.01 ± 0.05	1.50
Mancos Shale (perpendicular)	5	13	2.17 ± 0.01	0.03 ± <0.01	0.40
Mancos Shale (perpendicular)	6	17	2.17 ± 0.01	0.03 ± <0.01	0.74

Table 6: Parameter estimates and associated 95% confidence intervals obtained by fitting Eq. [4.1] to the neutron radiography data for each replicate of each rock group.

Rock type	Replicate number	Number of observations	Surface fractal dimension, D	Initial imbibition time, c (s)	RMSE (mm)
Burlington_Limestone	1	40	2.41 ± 0.01	0.03 ± <0.01	1.46
Burlington_Limestone	2	17	2.19 ± 0.01	0.01 ± <0.01	0.52
Burlington_Limestone	3	13	2.14 ± 0.04	0.01 ± <0.01	2.48
Burlington_Limestone	4	13	2.34 ± 0.06	0.01 ± <0.01	2.52
Burlington_Limestone	5	16	2.27 ± 0.04	0.03 ± <0.01	2.58
Burlington_Limestone	6	11	2.49 ± 0.01	0.01 ± <0.01	0.99
Burlington_Limestone	7	15	2.26 ± 0.03	0.01 ± <0.01	2.47
Sierra_White_Granite	1	23	2.35 ± 0.01	0.03 ± <0.01	1.40
Sierra_White_Granite	2	22	2.53 ± 0.01	0.02 ± 0.02	0.84
Sierra_White_Granite	3	32	2.34 ± 0.02	0.03 ± <0.01	1.93
Vermilion_Bay_Granite_B	1	85	2.33 ± 0.01	0.03 ± <0.01	1.41
Vermilion_Bay_Granite_B	2	26	2.34 ± 0.01	0.01 ± <0.01	1.63
Vermilion_Bay_Granite_B	3	59	2.30 ± 0.01	0.00 ± <0.01	0.90
Vermilion_Bay_Granite_B	4	70	2.40 ± 0.01	0.03 ± <0.01	1.56
Vermilion_Bay_Granite_B	5	38	2.11 ± 0.01	0.01 ± 0.01	0.76
Vermilion_Bay_Granite_B	6	35	2.22 ± 0.05	-0.03 ± 0.07	2.32
Vermilion_Bay_Granite_B	7	42	2.24 ± 0.02	0.03 ± 0.01	1.06
Vermilion_Bay_Granite_B	8	12	2.32 ± 0.01	0.03 ± 0.01	1.60
Vermilion_Bay_Granite_B	9	36	2.22 ± 0.01	0.03 ± 0.01	1.08
Vermilion_Bay_Granite_B	10	27	2.19 ± 0.01	0.01 ± 0.02	1.03
Vermilion_Bay_Granite_B	11	20	2.33 ± 0.01	0.02 ± 0.02	1.72
Vermilion_Bay_Granite_B	12	51	2.27 ± 0.01	0.01 ± 0.01	0.74
Westerly_Granite	1	28	2.32 ± 0.01	0.03 ± 0.01	0.71
Westerly_Granite	2	43	2.26 ± <0.01	0.03 ± <0.01	0.59

Table 7: Median values for estimated and measured parameters for all rock cores tested in both chapters 3 and 4.

Rock Type	Surface Fractal Dimension, D	Aperture Width†, $\overline{x}$ (μm)	Tortuosity†, τ	Replicates
Burlington Limestone	2.22	176	1.002	7
Crossville Sandstone	2.21	87	1.000	7
Mancos Shale (parallel)	2.35	124	1.006	7
Mancos Shale (perpendicular)	2.25	93	1.008	6
Sierra White Granite	2.27	231	1.003	3
Vermilion Bay Granite B	2.33	125	1.015	12
Westerly Granite	2.35	239	1.006	2

† Significant differences among rock types as indicated by Kruskal-Wallis test at $p < 0.05$

Appendix 2 - Figures

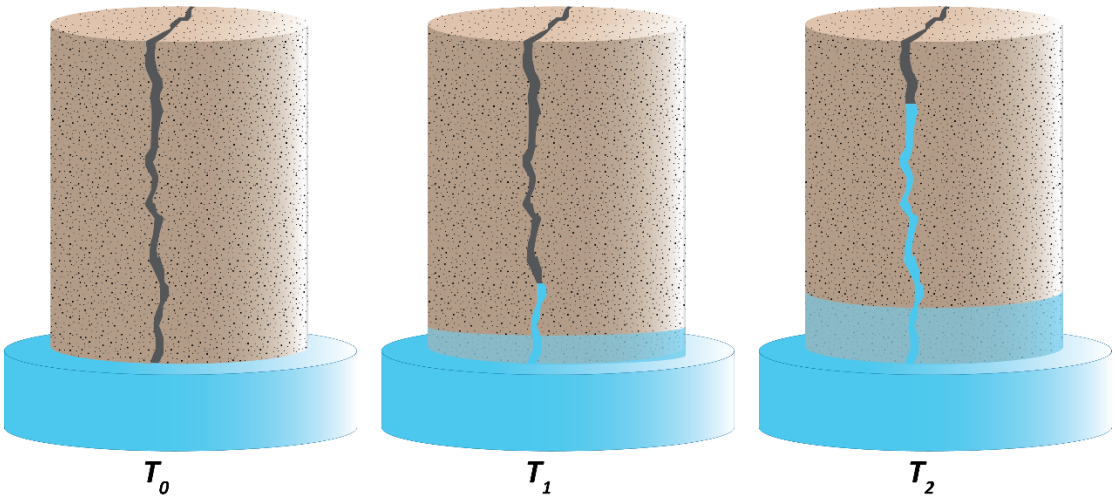

Figure 1: Illustration of a porous fractured core coming in contact with a water reservoir over time. T_0 indicates the initial contact of the core with the water reservoir shown on left. Later time steps T_1 and T_2 subsequently shown to the right. Spontaneous imbibition is shown as occurring both within the matrix and within the fracture. Note the difference in wetting front height between the fracture and matrix.

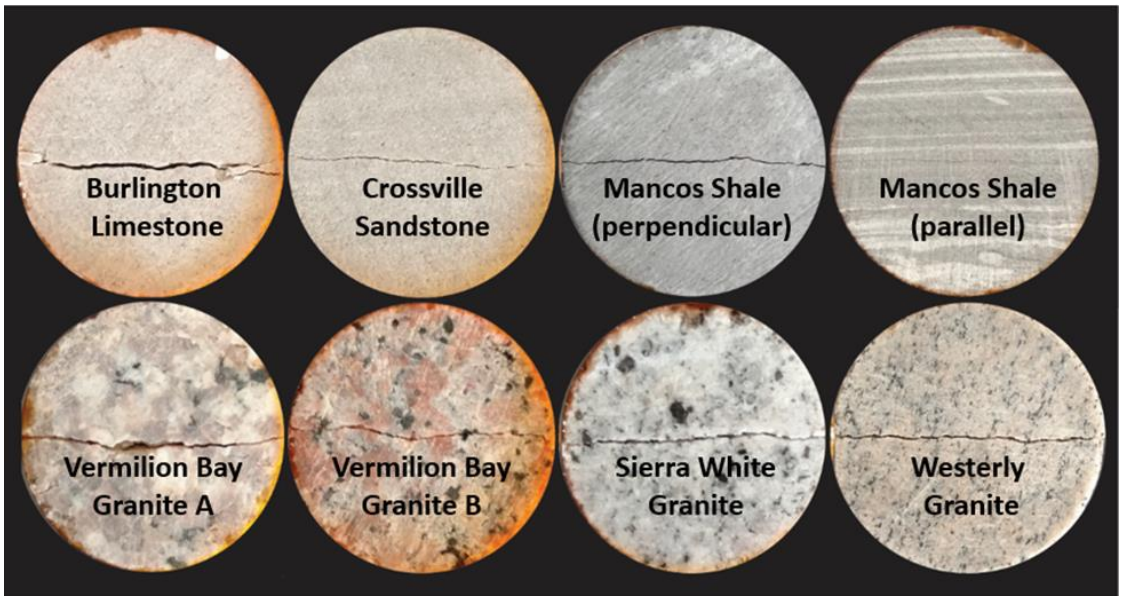

Figure 2 : Top view of fractured rock cores. Top row from left to right: Burlington Limestone, Crossville Sandstone, Mancos Shale (cored perpendicular), Mancos Shale (cored parallel); Bottom row from left to right: Vermilion Bay Granite A, Vermilion Bay Granite B, Sierra White Granite, Westerly Granite.

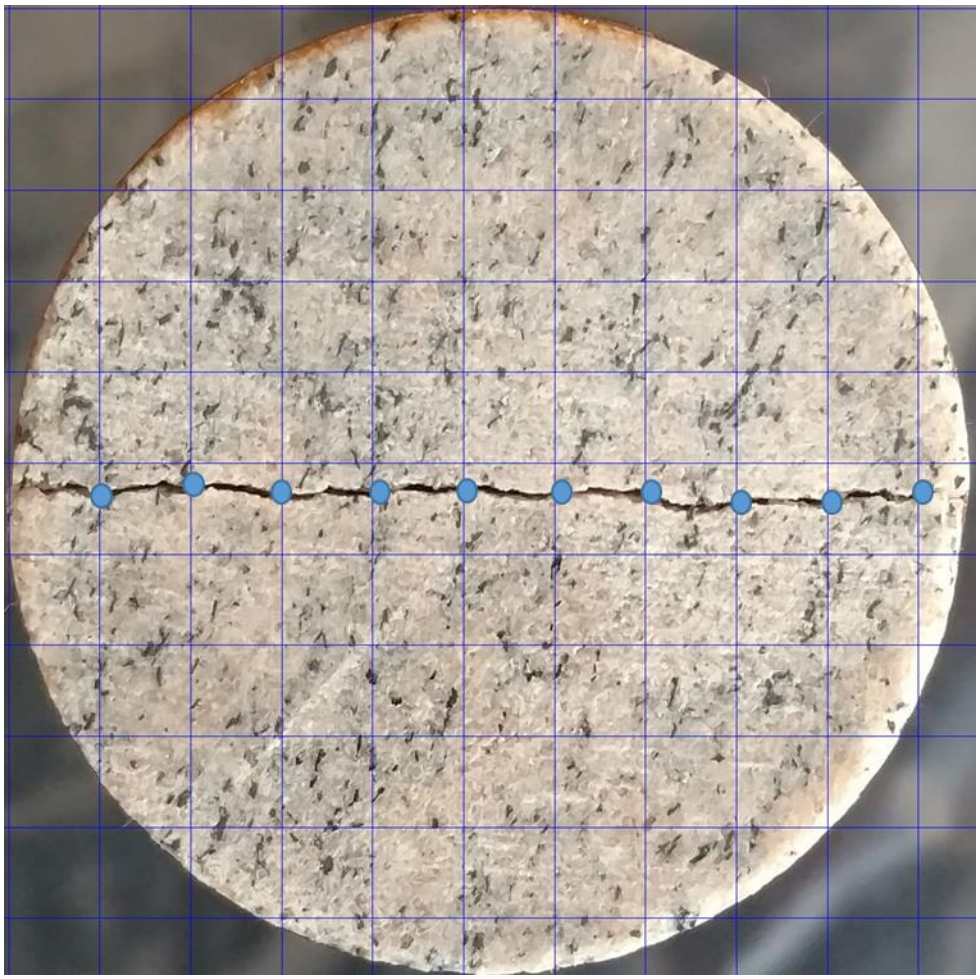

Figure 3 : Westerly Granite core with random overlying grid applied to image in ImageJ. Measurements taken at fracture intersection with grid as shown by blue points. Each core had two grids applied per core side resulting in 20 measurements per side and 40 measurements per core.

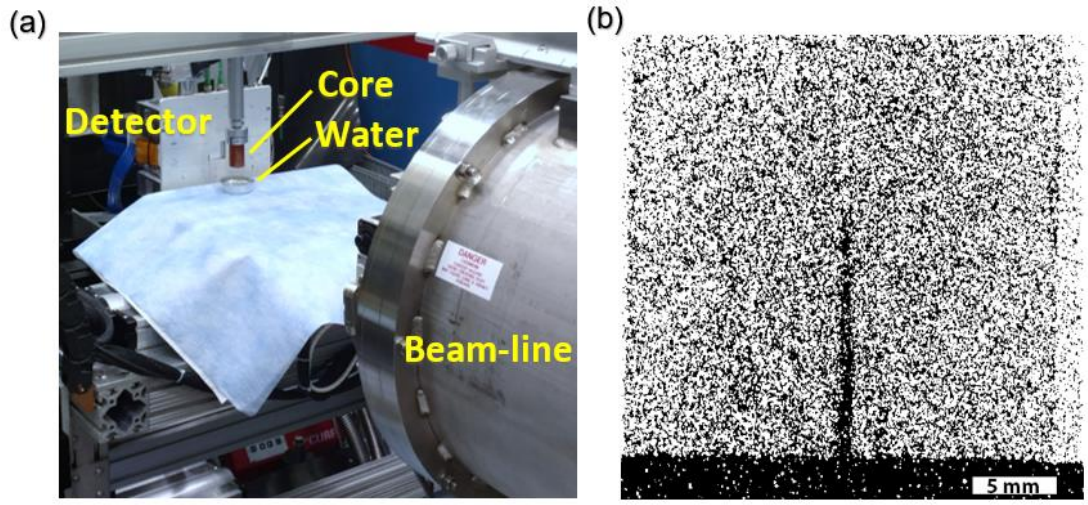

Figure 4 : (a) Neutron radiography imaging set-up with the MCP detector. The rock core (brown) is brought in contact with a water reservoir (aluminum container) in front of the beam-line while the detector images neutrons attenuated by the water. (b) Neutron radiograph produced by the MCP detector of a Crossville Sandstone sample. Note the water reservoir and the linear fracture imbibing water (black).

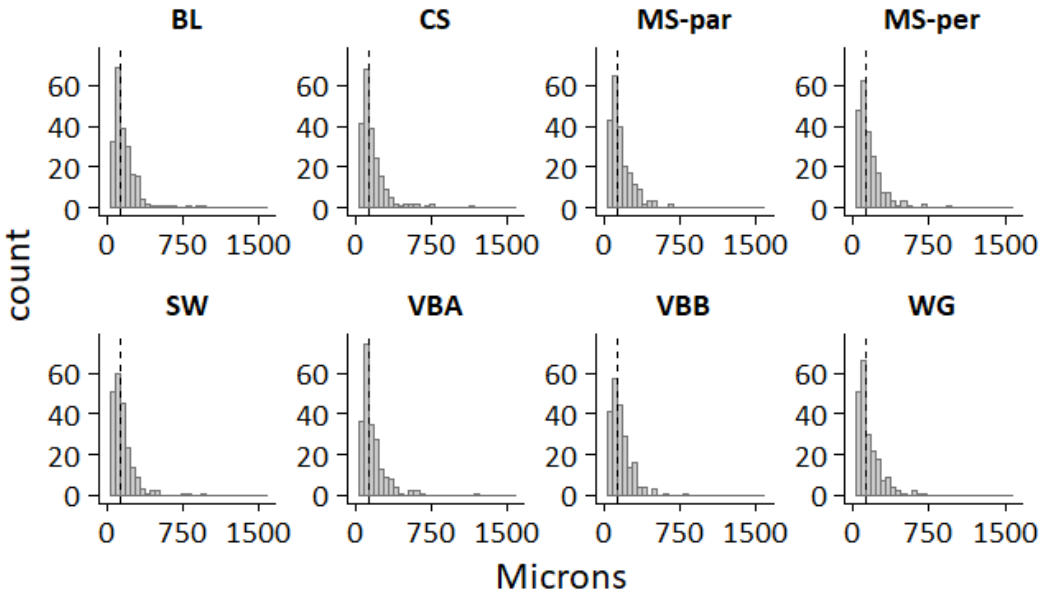

Figure 5 : Histograms showing the distribution of measured fracture aperture widths for each rock type. X-axis shows aperture width in microns and y-axis shows frequency. Geometric mean aperture width shown as a dotted black line. BL – Burlington Limestone, CS - Crossville Sandstone, MS-par – Mancos Shale (parallel), MS-per – Mancos Shale (perpendicular), SW – Sierra White Granite, VBA – Vermilion Bay Granite A, VBB – Vermilion Bay Granite B, WG – Westerly Granite. Note the right skewed distributions.

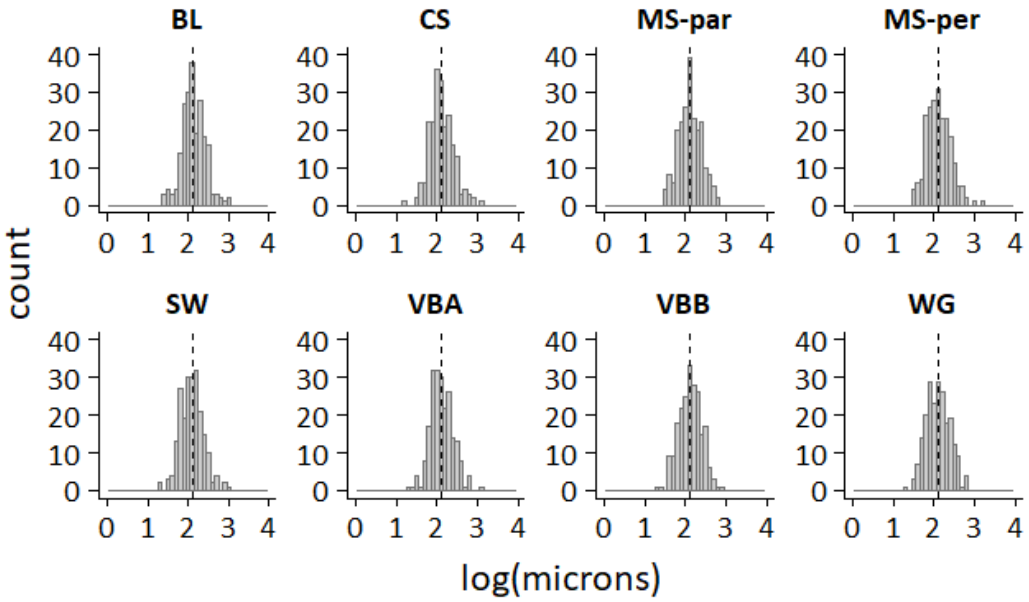

Figure 6 : Log-transformed distributions used for analysis of variance. X-axis is the logarithm of the aperture widths in microns. Y-axis represents the frequency. The arithmetic mean of the log distribution is shown as the black dashed line. BL – Burlington Limestone, CS - Crossville Sandstone, MS-par – Mancos Shale (parallel), MS-per – Mancos Shale (perpendicular), SW – Sierra White Granite, VBA – Vermilion Bay Granite A, VBB – Vermilion Bay Granite B, WG – Westerly Granite.

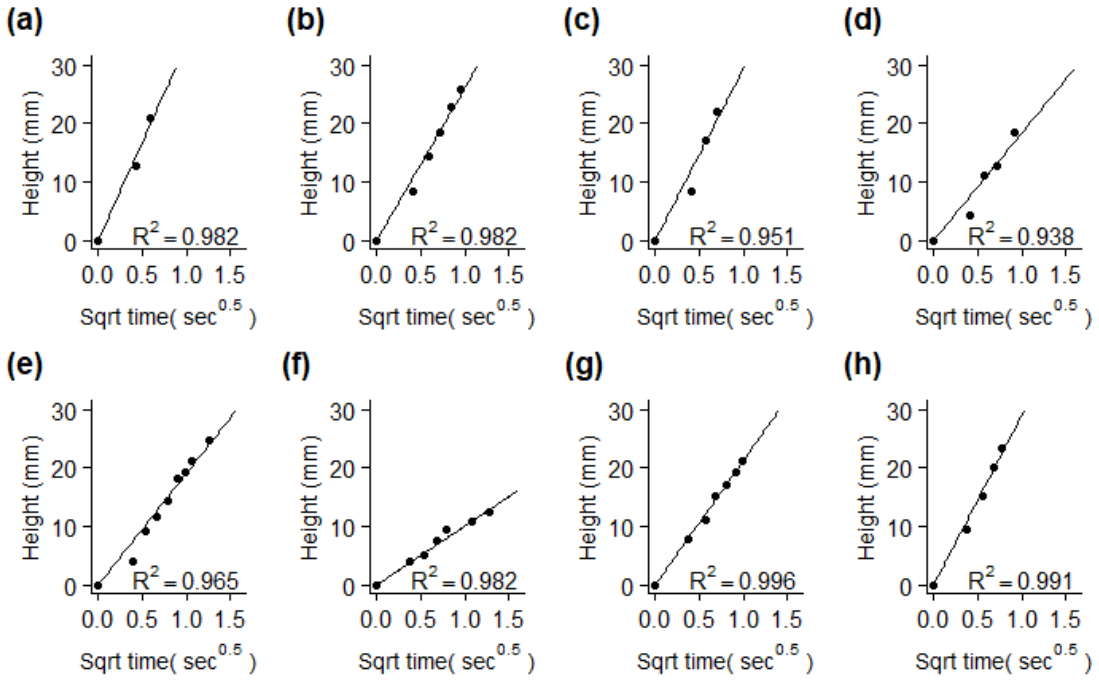

Figure 7 : Typical fittings of linear regression per rock type. The coefficient of determination R^2 is shown for each rock type. X-axis represent the square root of time and Y-axis represents the wetting height in mm. The slope of each regression line is equivalent to the respective sample's sorptivity. a) Burlington Limestone; b) Crossville Sandston; c) Mancos Shale (parallel); d) Mancos Shale (perpendicular); e) Sierra White Granite; f) Vermilion Bay Granite A; g) Vermilion Bay Granite B; h) Westerly Granite.

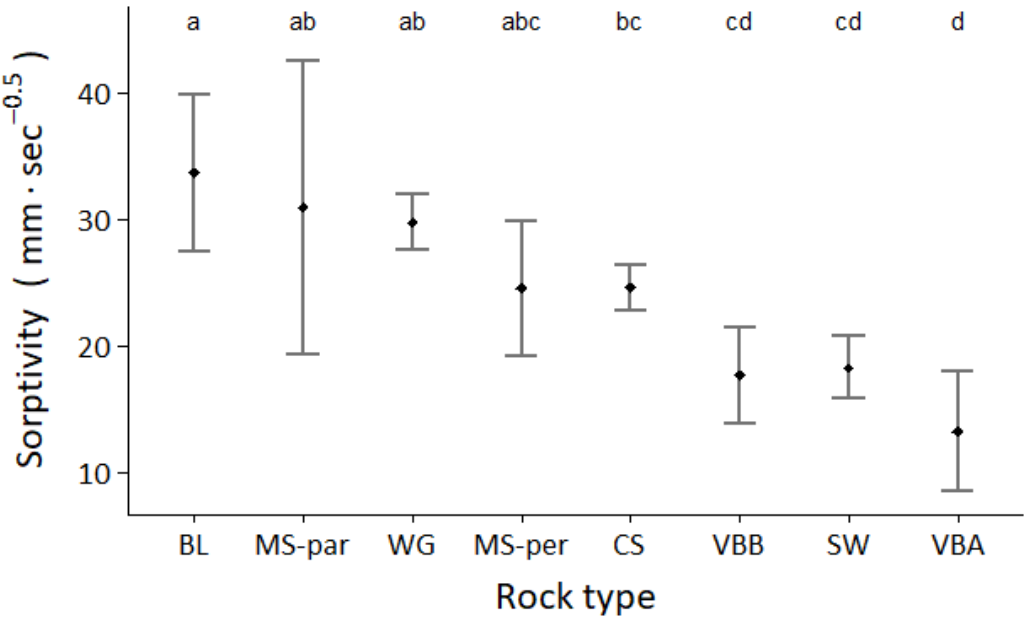

Figure 8 : Mean fracture sorptivity with 95% confidence intervals and Tukey letter groupings shown for each rock type. Y-axis is sorptivity in $mm \cdot sec^{-0.5}$. The arithmetic average of each distribution is shown as a black diamond. Rock types with the same Tukey letter are not significantly different. BL – Burlington Limestone, MS-par – Mancos Shale (parallel), WG – Westerly Granite, MS-per – Mancos Shale (perpendicular), CS - Crossville Sandstone, VBB – Vermilion Bay Granite B, SW – Sierra White Granite, VBA – Vermilion Bay Granite A.

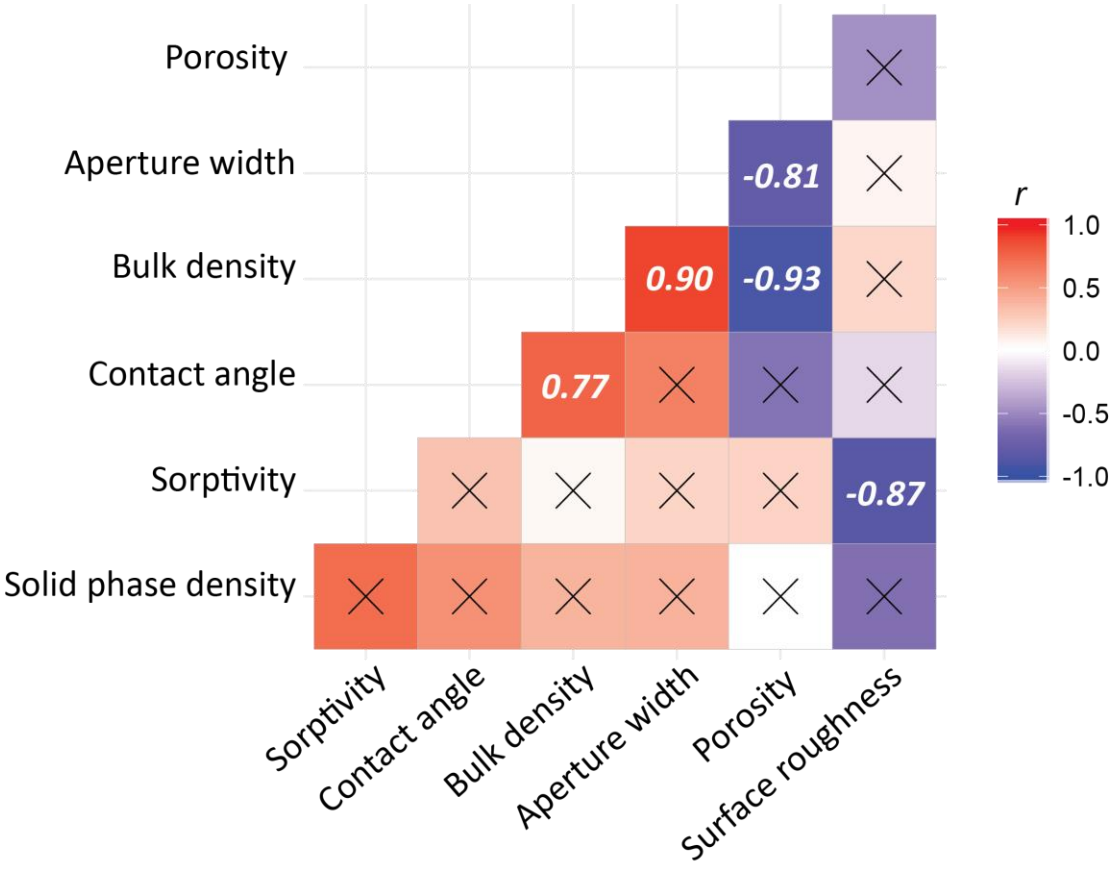

Figure 9: Correlation matrix illustrating relationships between sample rock properties. Values of bulk and solid phase density as well as porosity were measured by Andrew Vial. Measurements of contact angle and roughness from Gates (2018). No significant relationship designated by an "X." Positive correlations shown in red with negative correlations shown in blue with gradations in color indicating the strength of correlation coefficient (r). Significant relationships at $p < 0.05$ shown with value of correlation coefficient (r).

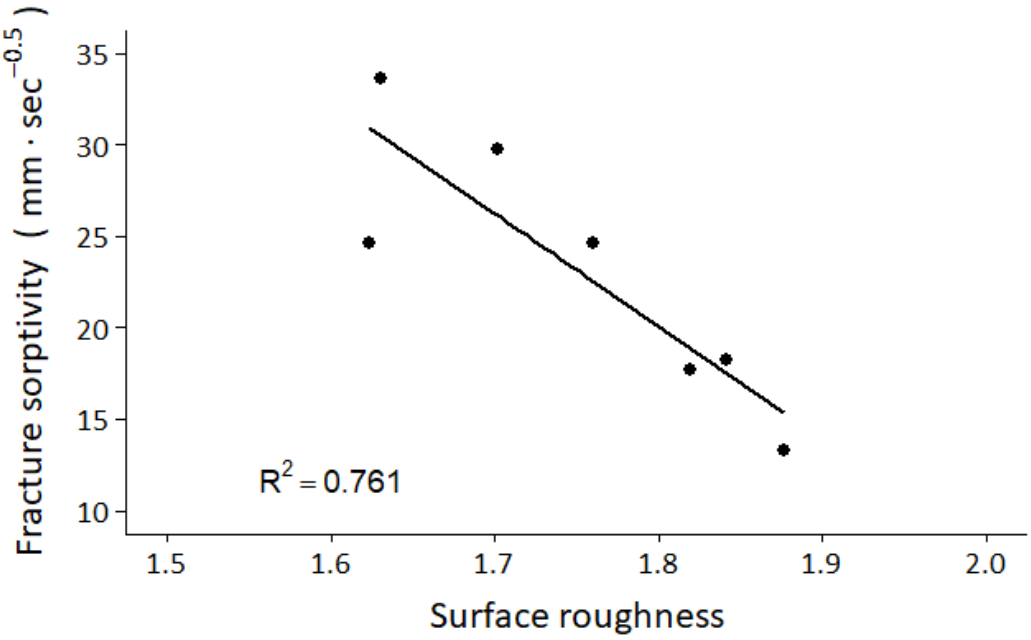

Figure 10: Linear regression relationship between measured fracture sorptivity values and Wenzel surface roughness for all rock types. Roughness measurements from Gates (2018).

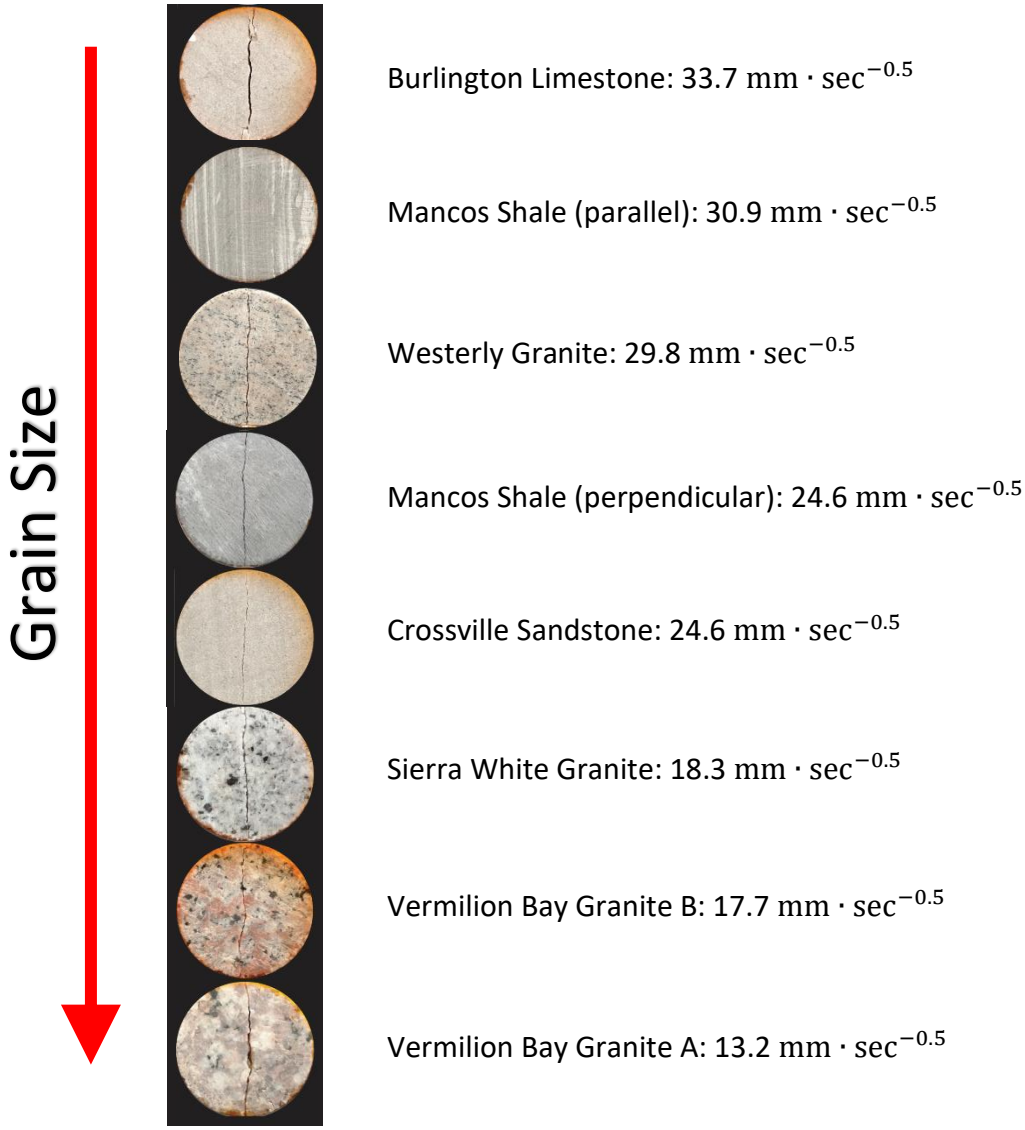

Figure 11: Core samples ordered from highest sorptivity (top) mm · sec$^{-0.5}$ to lowest (bottom). General qualitative negative correlation shown between increasing grain size and decreasing sorptivity values. Note that this trend seems to fit to all rock types except the Westerly Granite, which has a larger grain size relative to other rock types as well as a higher sorptivity.

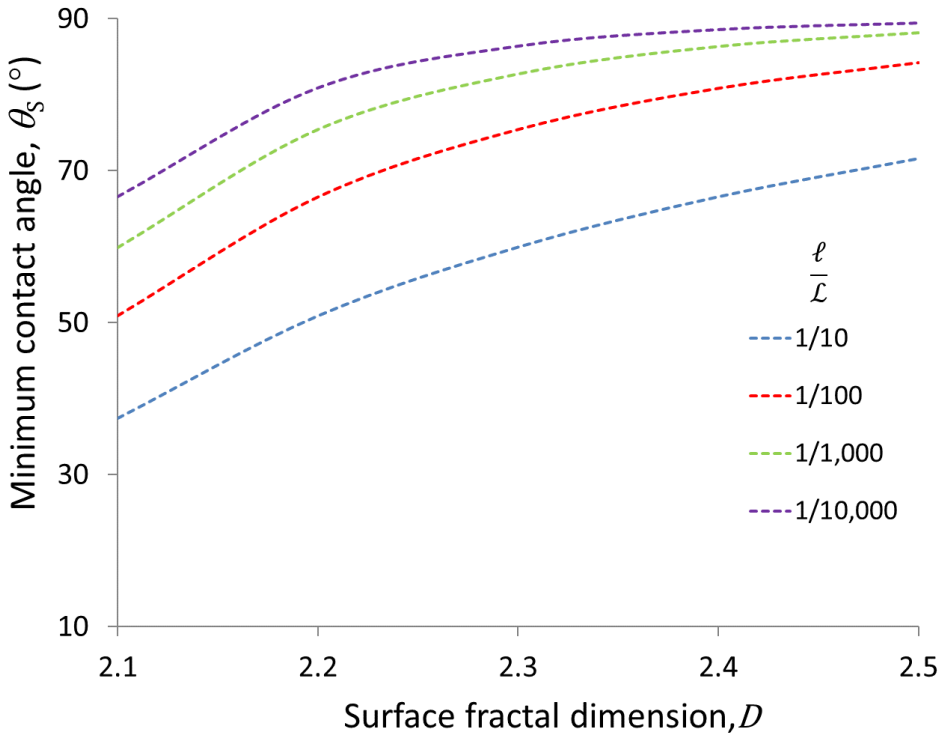

Figure 12: Minimum contact angles for a fluid on a smooth flat surface, θ_S, required to give $\theta_R > 0$ on a rough fractal surface predicted using Eq. [3.7] for various combinations of D and $\frac{\ell}{\mathcal{L}}$.

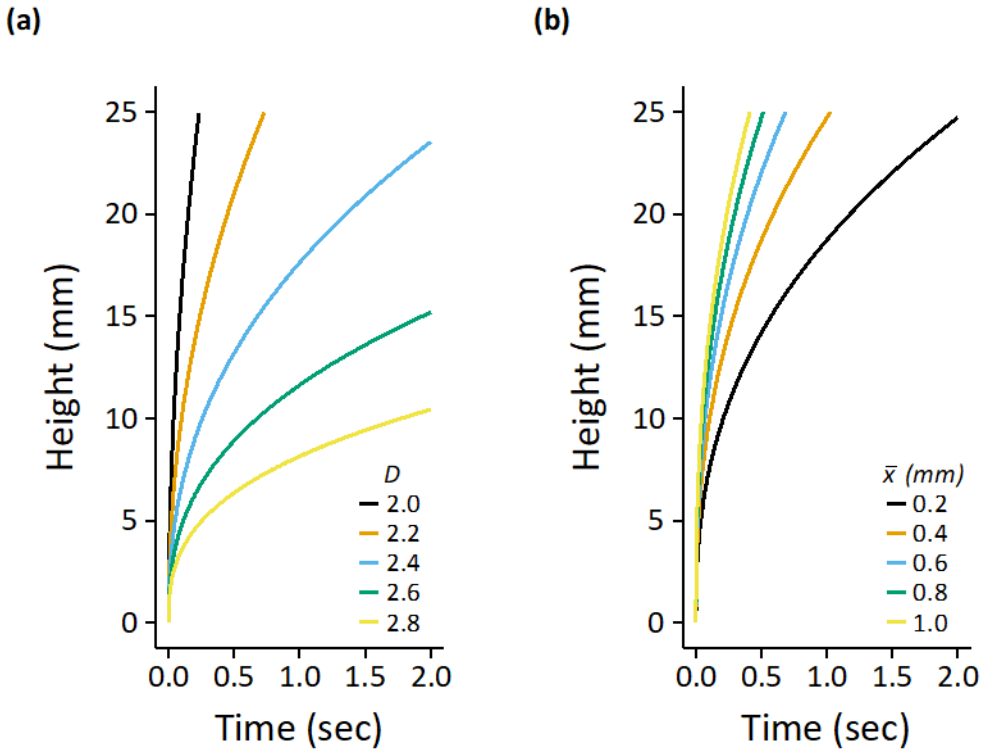

Figure 13: Height of wetting within a fracture versus time as predicted by Eq. [3.12]. (a) Fracture aperture spacing, $\bar{x}$, held at 100 μm while varying the surface fractal dimension, D. (b) Surface fractal dimension D held at 2.5 while varying the fracture aperture spacing, $\bar{x}$.

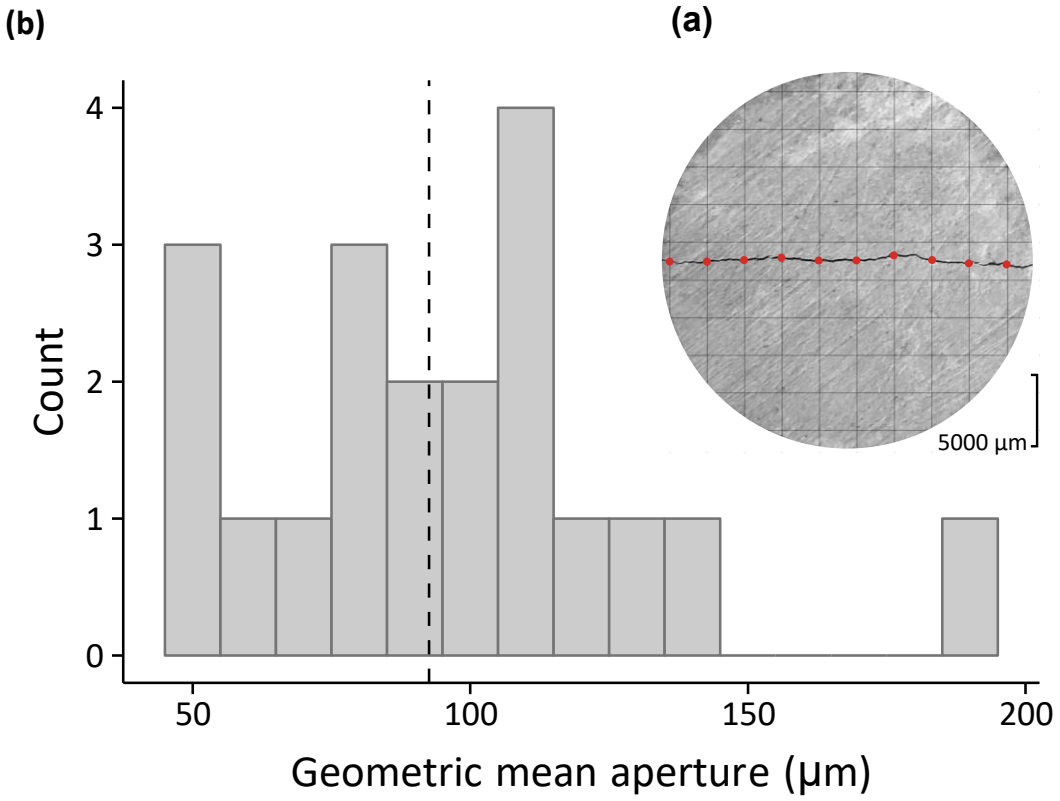

Figure 14 : (a) A typical fractured Mancos Shale (perpendicular) core shown with a superimposed random grid; measurements of aperture width were taken at the intersection points of the fracture and the grid (shown as red dots). (b) Frequency distribution of geometric mean fracture aperture widths for all of the rock types (20 cores) with a bin size of 10 µm; the vertical dashed line represents the median value.

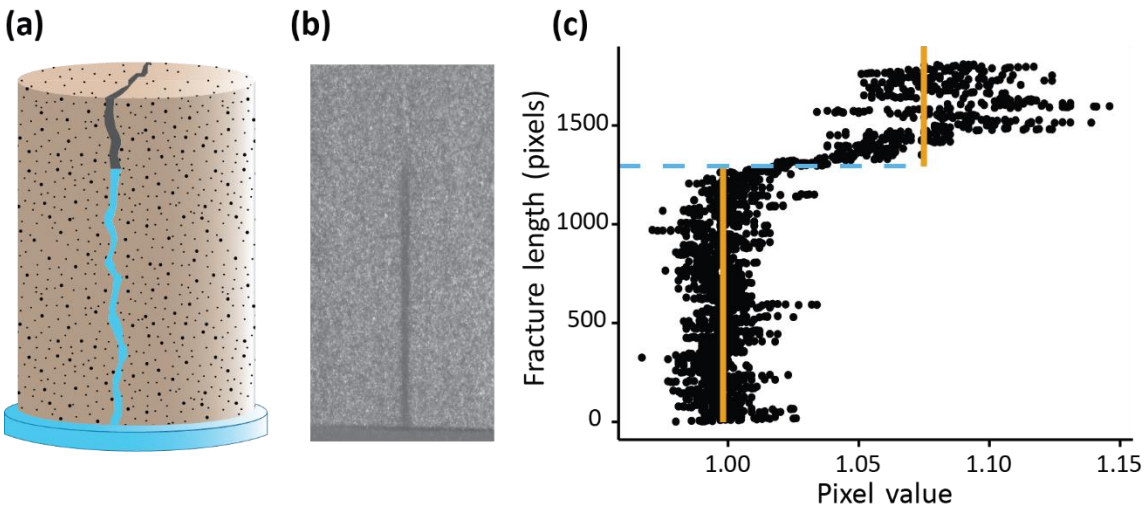

Figure 15 : (a) Schematic illustration showing the uptake of water within a fractured core sample soon after basal contact with water. (b) Example of a normalized neutron radiograph showing water (in black) within a fractured Crossville Sandstone core. (c) Change point analysis of the neutron radiograph shown in b. The solid orange lines represent mean pixel values for the wet and dry regions within the fracture. The blue dashed line is the detection point, representing the height of wetting, at which a shift in the mean pixel values occurred.

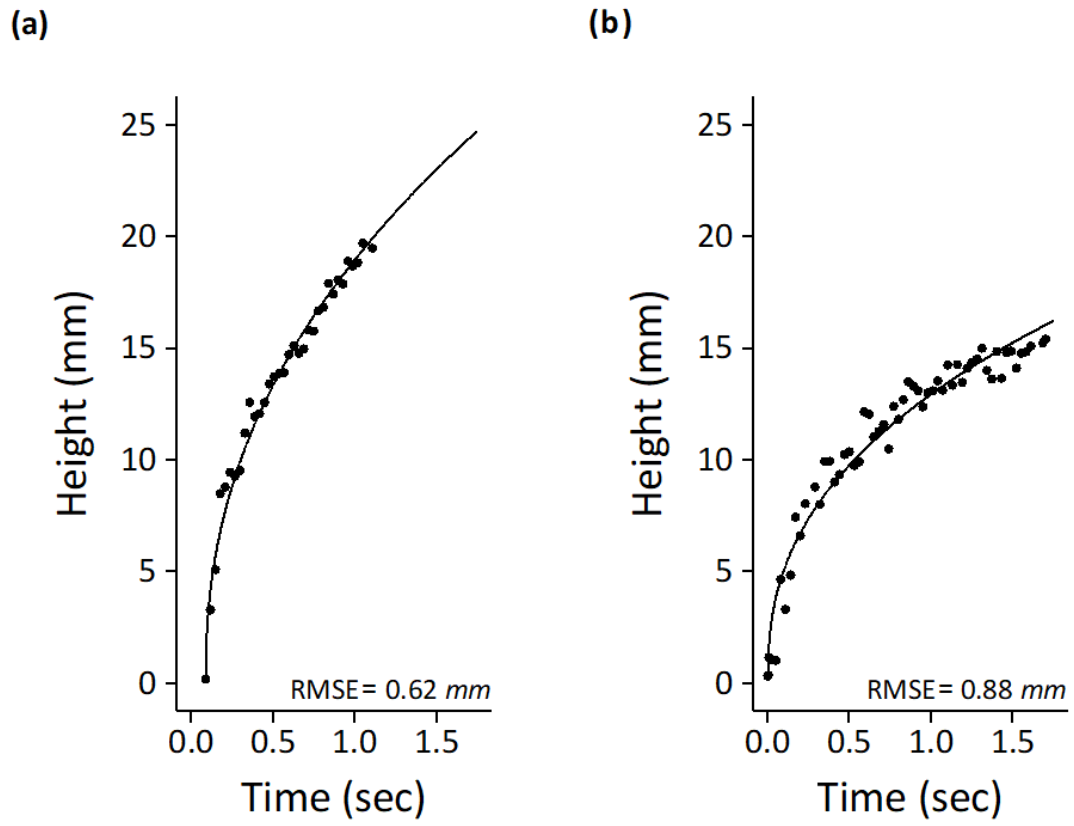

Figure 16 : Typical height of wetting versus time data sets determined using dynamic neutron radiography and change point analysis: (a) Crossville Sandstone, replicate number 3, and (b) Mancos Shale (cored parallel to bedding), replicate number 2. The solid lines represent predicted values obtained from fitting of Eq. [3.13] to the experimental data using non-linear regression.

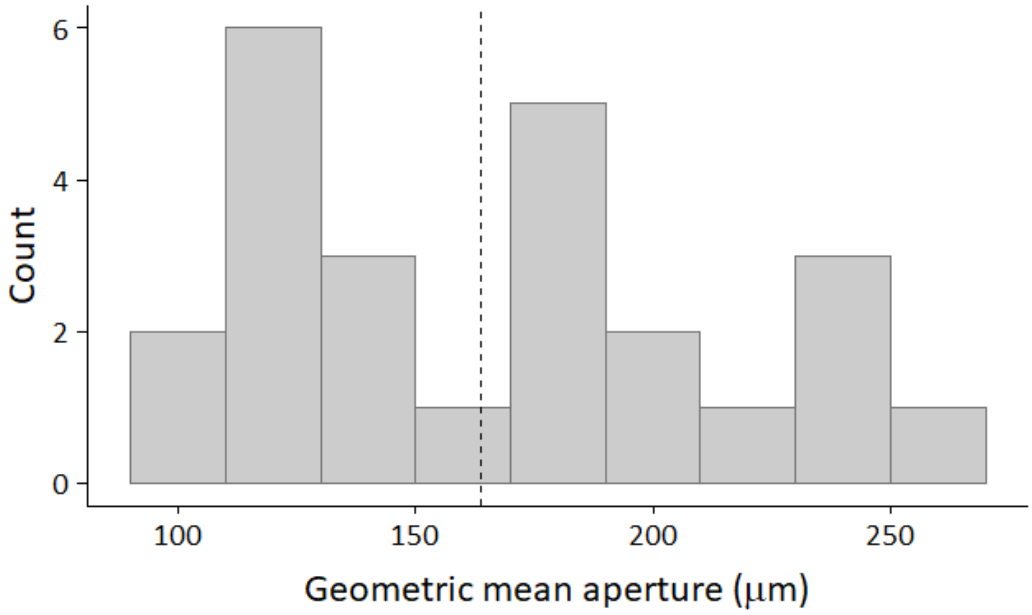

Figure 17 : Frequency distribution of geometric mean fracture apertures for all of the rock types (24 cores) with a bin size of 20 μm; the vertical dashed line represents the median fracture aperture.

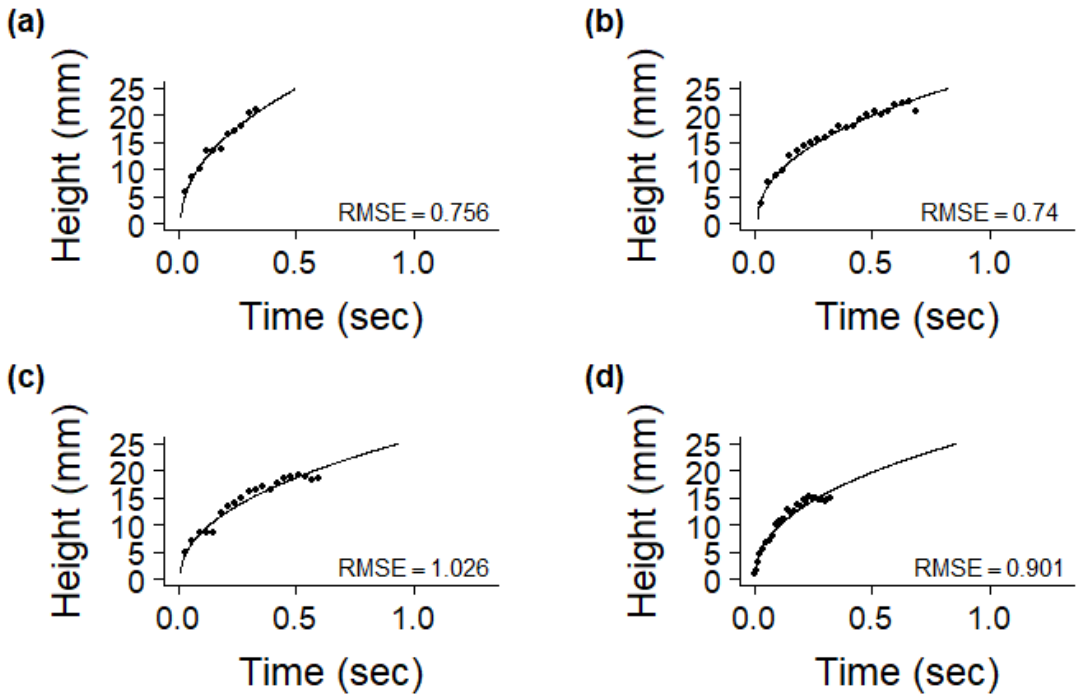

Figure 18 : Typical height of wetting versus time data sets determined using dynamic neutron radiography and change point analysis: (a) Burlington Limestone, replicate number 3, (b) Sierra White Granite, replicate number 2, c) Vermilion Bay Granite B, replicate number 11, and d) Westerly Granite, replicate 1. The solid lines represent predicted values obtained from fitting of Eq. [4.1] to the experimental data using non-linear regression.

Vita

Jared William Brabazon was born in Beloit, Wisconsin to Gary and Debra Brabazon; he has two older brothers, Matthew and Joshua, and one older sister, Stephanie. Jared attended Turner High School in Beloit, WI graduating in 2009. From there, he served a two year volunteer mission in the country of Latvia, where he became fluent in the native language of Latvian and was able to devote his time to providing service to those in need. Jared then attended Brigham Young University in Provo, Utah where he met his wife, Holly. He graduated with his B.S. in Geology in 2016. In the spring of 2017, Jared entered the graduate program in the Department of Earth and Planetary Sciences at the University of Tennessee in Knoxville, Tennessee. Jared graduated with a Master of Science Degree in Geology in August 2018.